DESIGN AND FABRICATION OF GUIDED-MODE RESONANCE DEVICES

by

GUOLIANG CHEN

Presented to the Faculty of the Graduate School of

The University of Texas at Arlington in Partial Fulfillment

of the Requirements

for the Degree of

DOCTOR OF PHILOSOPHY

THE UNIVERSITY OF TEXAS AT ARLINGTON

December 2015

Acknowledgements

I express my deep appreciation to my advisor, Dr. Robert Magnusson, who continuously guided and supported me throughout my Ph. D period. His broad and deep knowledge in optics helped me overcome many difficulties in this area and in the end to make this dissertation accomplished. I gained a lot from his research guidance and valuable courses. Also, his attitude of research and teaching were very helpful to me.

I would like to take this opportunity to thank the University of Texas at Arlington and the Electrical engineering department for their supports. Thanks are also due to my graduate committee members, Dr. Kambiz Alavi, Dr. Samir Iqbal, Dr. Michael Vasilyev and Dr. Yuze (Alice) Sun. Not only did they provide good suggestions for my dissertation, but also worthy courses which helped me to build foundation of my knowledge system.

I need to thank my group members, especially Dr. Jay Yoon and Dr. Kyu Lee. I can always receive your unselfish help whenever I need it; every discussion or argument was helpful. And I also thank my friends and colleagues from NanoFAB.

I am very grateful to my parents: Yunxuan Chen, Lijun Peng and my wife Yi Li. You are always the great supporters for me during this long and uneasy journey.

November 5, 2015

Abstract

DESIGN AND FABRICATION OF GUIDED-MODE RESONANCE DEVICES

GuoLiang Chen, PhD

The University of Texas at Arlington, 2015

Supervising Professor: Robert Magnusson

Guided-mode resonance (GMR) effect based on waveguide grating structure has been attracting plenty of attention in recent years due to its abundant application in energy, information technology, and sensors. This dissertation aims to develop new GMR devices and apply them in the above fields.

Initially thermoelectric devices integrated with optical resonance absorbers are demonstrated. We design the absorbers with rigorous numerical methods and fashion experimental prototypes by thin-film deposition, patterning, and etching. A ~2.5-μm-thick p-type heavily doped polysilicon film on a ~2-μm layer of thermally grown SiO_2 enables guided-mode resonance. The SiO_2 layer additionally serves to thermally insulate the polysilicon layer from the Si substrate. A grating layer is etched into the polysilicon film to form the absorber. Thus, the polysilicon film works as a functional material for both the absorber and the thermoelectric converter itself. Numerical simulations show that the resonance segment enhances absorption by ~30% in the visible spectral range and by ~40% in the infrared range relative to unpatterned devices. Moreover, experimental results demonstrate significantly increased electrical output over reference devices. These simple devices can be applied as compact voltage generators and IR sensors.

Thereafter GMR multiline devices are investigated. As a preliminary study, a glass-sub multiline guided-mode resonance (GMR) filter is applied as a reflector in order

to implement an external cavity laser. We design the resonant element using rigorous numerical methods and fashion an experimental prototype by thin-film deposition, patterning, and etching. A ~100-nm TiO_2 grating layer on a ~170-μm-thick glass slab supports thousands of resonant modes. We detect ~10 narrow resonance peaks within a ~10-nm wavelength range centered at the 840-nm wavelength. We apply this multiline GMR device to a gain chip and obtain several simultaneous resonant laser lines that compete for the gain. Precise tuning enables a stable laser line that can be selected from the multiple available resonant lines.

Furthermore we investigate GMR multiline devices in more detail and with better performances. GMR multiline filters exhibiting resonance lines on a dense spectral grid in a broad near infrared (NIR) wavelength range are demonstrated. We design the filters using rigorous numerical methods and then proceed with experimental verification by patterning, etching, and collecting spectral data. In one embodiment, we design and fabricate thick Si slab-based multiline filters within a wavelength range centered at the 1550 nm with potential application in high sensitivity gas sensors and signal processing system. Devices with two types of gratings, Si grating and TiO_2 grating, are demonstrated experimentally with TiO_2 grating devices exhibiting better performances. For TiO_2 grating devices we can detect 12 narrow resonance peaks within a 10 nm wavelength range centered at the 1550 nm. The spectral width of each resonance peak is ~0.1 nm with free spectral range of ~0.8 nm. High efficiency of ~0.9 and low sideband of ~0.01 can be obtained for individual device output. Design of polarization independent multiline filter and Brewster multiline filter are also presented.

Finally, we apply GMR devices to implement the return-to-zero (RZ) and non-return-to-zero (NRZ) formats conversion. We realize the conversion by two solutions. For solution one RZtoNRZ conversion is done by 2 cascading filters – GMR multiline filter

and Gauss filter. We simulate the complete conversion flow using MATLAB where the spectral data of the GMR multiline device is directly input into the MATLAB codes. We successfully obtained a converted NRZ signal. For solution two we prove that an individual filter possessing Gaussian shape can also realize the conversion. Furthermore we design GMR filters to possess spectral shape matched to the referred optimal FBG filter spectrum. By doing this we can theoretically prove that one individual GMR filter (reflection or transmission) can implement RZtoNRZ conversion with good performance.

Table of Contents

List of Illustrations

List of Tables

Chapter 1

Introduction

1.1 Background

Optics and photonics have been actively researched over a long history of time [1]. Resonance effects of various origins constitute the basis for optical and photonic devices engineering in a broad context. Particularly, the guided-mode resonance (GMR) effect based on waveguide grating structure has been attracting plenty of attention in recent years [2,3,4,5] due to its abundant application in energy [6], information technology [5,7] and sensors [8]. Various models and numerical methods such as rigorous coupled-wave analysis (RCWA) have been developed to understand and describe this optical phenomenon [9,10]. Up to date, the depth and breadth of research in this field have been enormous. In this dissertation we continue the endeavor to explore new GMR devices and applications as in: GMR coupled thermoelectric device with application in voltage generation and IR sensing, multiline thick GMR devices with application in laser, gas sensor and signal processing, and GMR reflection / transmission devices applied in return to zero (RZ) to non-return to zero (NRZ) signal conversion are investigated. In energy field, much effort has been made to efficiently convert electromagnetic radiation into applicable electrical output. Daniel et al. experimentally demonstrated one solar thermoelectric generator with a selective absorber [11]. Ogawa et al. reported an IR thermoelectric sensor with plasmonics photonic crystal absorber [12]. Here GMR structure is employed as an efficient light absorber to enhance the electrical output. In the field of optical signal and system filtering useful spectra is a fundamental function thus can be applied in various areas. Often a single resonance of filtering in a given spectral band is sufficient to design useful devices [8]. In contrast, multichannel filters passing or blocking selected sets of wavelengths are of interest, for

example, arrayed waveguide gratings in telecommunication systems [13]. Whereas periodic resonance elements supporting a single, or a few, resonance lines have been widely studied in nanoplasmonics and nanophotonics; less effort has involved multiline devices. In this dissertation, we aim to design and fabricate multiline GMR devices that possess multiple resonance peaks and discuss their possible applications. Finally, we investigate the implementation of RZ to NRZ conversion using GMR reflection and transmission devices.

GMR effect is based on the diffraction and interference of light in the waveguide grating structure. Considering zero order regime the subwavelength diffraction grating not only reflects and transmits zero order light but also diffracts higher order evanescent light into the waveguide layer. When the propagating waveguide mode is reradiated by the diffraction grating, called leaky mode, by phase matching condition they can have constructive or destructive interference with the zero order reflected or transmitted beam thus GMR occurs. The basic equations for the grating and phase matching are as following:

$$n_P \sin \theta_{P,i} = n_C \sin \theta_{in} - i \lambda_0 / \Lambda \qquad (1.1)$$

where λ_0 is the free space wavelength, i is an integer, P is either C or S depending on the region under consideration.

$$\beta_{i,\nu} = k \left(n_c \sin \theta - i \frac{\lambda}{\Lambda} \right) \qquad (1.2)$$

where i is the harmonic order, ν is the mode index, Λ is the period, $k = 2\pi/\lambda$, λ is the free space wavelength. n_c is the refractive index of cover medium, θ is the incident angle.

Classical GMR structure consists of a subwavelength periodic grating and a waveguide over a substrate as shown in Figure 1-1(a) with period Λ, fill factor F, grating depth d_g, waveguide thickness d_w, incident beam I, reflected beam R, and transmitted beam T. The grating layer can act as the coupling as well as waveguide layer. At

resonance, diverse spectral characteristics in both reflection and transmission can be obtained as for one example shown in Figure 1-1 (b). Depending on the wavelength, incident angle and device parameters designed by RCWA the spectral bands of these resonant leaky-mode elements can be engineered for various optical and photonic device applications.

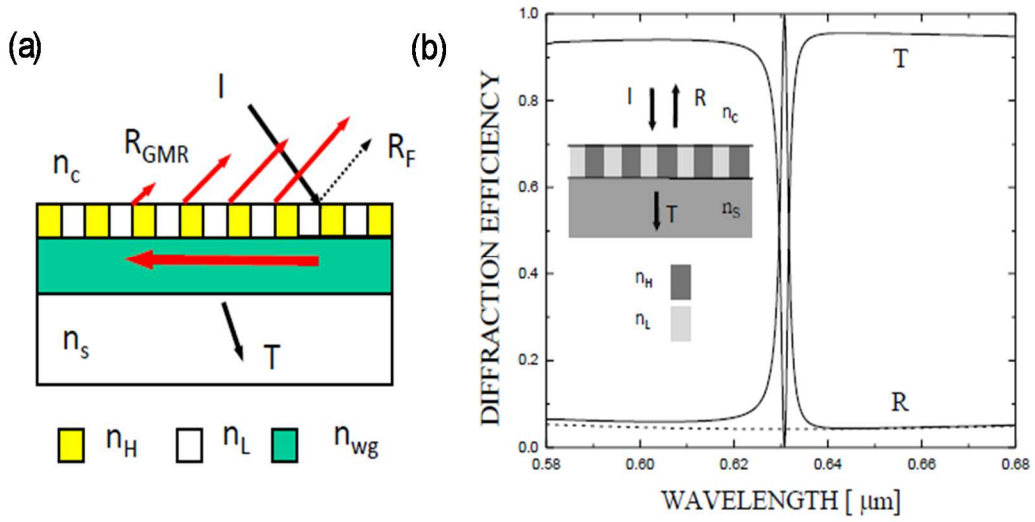

Figure 1-1 Schematic view of (a) classical GMR element and (b) spectral response. We consider zero-order grating and in the waveguide grating structure $n_w > n_{g,\,av} > n_c > n_s$; R_{GMR} is the GMR component of reflection and R_F is the Fresnel component of reflection with $n_{g,\,av} = N_{eff}$ [7, 10].

1.2 Overview of the Dissertation

In this dissertation, we investigate new types of GMR devices and their applications.

In Chapter 2 GMR coupled thermoelectric devices are designed and fabricated. In this device the GMR element works as a new light absorber to enhance the light absorption within visible and IR wavelength range. P-type heavily doped polysilicon is

employed for both GMR absorber and thermoelectric module thus integrate them together. The reason we choose this material is due to its high Seebeck coefficient and low cost. We use particle swarm optimization (PSO) to optimize the GMR parameters for maximum absorption and rigorous coupled-wave analysis (RCWA) to simulate the absorption enhancement ratio with comparison to unpatterned devices. Thereafter fabrication, characterization and test of the GMR devices are presented and compared to unpatterned devices. Experimental results demonstrate that GMR devices can significantly enhance the useful electrical output compared to unpatterned devices. The preliminary results we achieved provide a good alternative and more design freedom for application in voltage generator and IR sensors.

Chapter 3 addresses multiline thick GMR devices and their applications as laser mirrors. A recent study furnished a quantitative evaluation of the resonance properties of very thick resonance elements [14]. Motivated by these preliminary results we explore this type of new GMR devices profoundly and comprehensively. Based on the application of multiline laser mirror we design a glass-based near IR resonant reflector using rigorous coupled-wave analysis (RCWA) and fabricate the multiline mirror. The resulting filter possesses a dense population of resonant states with relatively narrow resonance bandwidths of individual spectral lines. We apply it to an electrically pumped gain medium and achieve selective laser lines that correspond to the dense resonance peaks generated by the mirror. We implement both mode-competing laser lines and stable single laser line experimentally.

In Chapter 4, considering the potential application in high sensitivity gas sensors and optical communication, we investigate multiline devices in more details. We employ a thick Si waveguide layer that can support thousands of modes; the grating structures include both Si grating and TiO_2 grating. We realize practical designs with well-shaped

resonance spectra using RCWA. We fabricate the designed filters and compare experimental performance with theoretical predictions in the telecommunications spectral region. Experimental results demonstrate that there is reasonable match between theory and experiment. We also study polarization independent devices. Furthermore, we investigate the angular characteristics of multiline filter devices. A Brewster multiline filter is implemented with extremely narrow linewidth and low, flat sideband. By cascading two similar multiline devices with a proper incidence angle we can achieve better spectral performances. The FWHM linewidth can be reduced by ~ 25% and the sideband can be lowed by ~ -10 dB at the expense of peak efficiency dropping by ~ 0.1 compared with individual device. This low sideband and narrow band spectrum has great potential application in optical communication and high sensitivity gas sensor. Another angular characteristic is the resonance peak angular shift. Experiments demonstrate the resonance peak move from ~ 1551nm to ~ 1552nm, i. e. one FSR when incidence angle changes from 9.92° to 10.15°. That shows reasonable agreement with the simulated spectra.

Chapter 5 discusses, theoretically, the implementation of RZ-to-NRZ signal conversion in optical communication by employing GMR devices. We realize the conversion by 2 solutions. In solution 1 RZ-to-NRZ conversion is done by 2 cascading filters – GMR multiline filter and Gauss filter. We simulate the complete conversion flow using MATLAB and the spectral data of GMR multiline device is directly input into the MATLAB codes. We successfully obtain converted NRZ signal. In solution 2 we prove that an individual filter possessing Gaussian shape can also realize the conversion. Furthermore we design the GMR filter to possess spectral shape matched to the referred optimal FBG filter spectrum. By doing this we can theoretically prove that one individual

GMR filter (reflection or transmission) can implement RZtoNRZ conversion with good performance.

Finally, Chapter 6 draws the conclusions based on all the results from previous chapters and also points out future research directions.

Chapter 2

Thermoelectric Devices Incorporating Photonic Resonance Segments

2.1 Introduction

Energy conversion applying thermoelectric materials and devices is of interest in numerous practical situations [15,16]. Since the discovery of the Seebeck effect in 1821, thermoelectric phenomena have been widely researched and applied to convert heat into electricity. The requisite thermal gradients can be induced for example by visible sunlight, infrared (IR) radiation, and many forms of wasted heat. Thermoelectric devices can work as solar cells, IR sensors, and energy harvesters. Device architecture in the form of metal-semiconductor-metal is capable of generating a Seebeck voltage, as discussed in depth by Wang [17]. An essential fact is that this device class operates in the presence of a temperature gradient such that the two metal contacts are held at different temperatures.

Common thermoelectric devices include two fundamental functional modules, namely the absorber and the thermoelectric converter. Numerous published papers address different approaches to implement these modules. For example, Kraemer et al. experimentally demonstrated a solar thermoelectric generator with a selective absorber [18]. Ogawa et al. reported an IR thermoelectric sensor with a plasmonic photonic crystal absorber [19]. Xu et al. presented an IR detector employing a dielectric stacked layer as the absorber [20]. Mizoshiri et al. demonstrated thin-film thermoelectric modules operating under focused sunlight [21] whereas Weinstein et al. provided numerical modeling of these types of devices [22]. In practical thermoelectric converters, thermocouples or thermopiles are generally adopted to convert input heat into electricity [18-23]. Figure 2-1 shows some state-of-the-art thermoelectric devices.

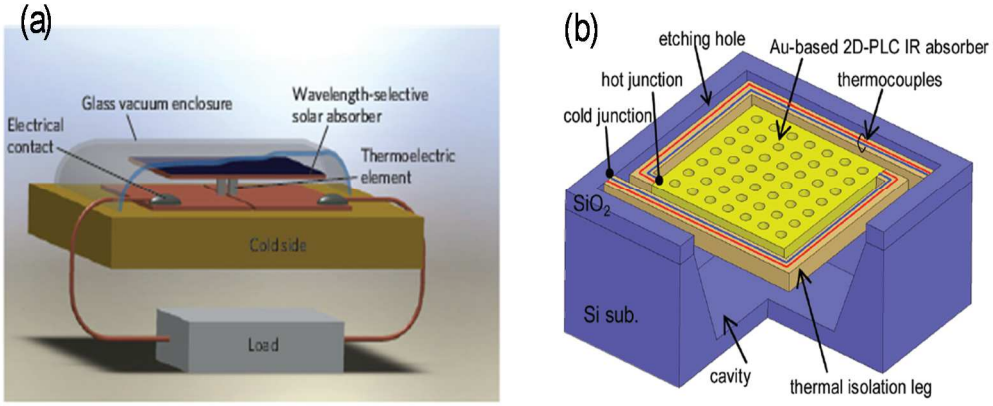

Figure 2-1 State-of-the-art thermoelectric devices [18, 19].

In this Chapter, we investigate an approach to induce absorption and to establish a thermal gradient via photonic resonance effects in thin-film thermoelectric generators. We present examples of resonance-coupled thermoelectric devices that work within the visible- and IR-wavelength ranges and suggest that they can be applied as compact, planar voltage generators and IR sensors.

Numerous device concepts in nanophotonics and nanoplasmonics operate under intricate resonance effects generated with nanopatterned films. If the incident light couples strongly to the film concomitant resonance effects impose diverse spectral signatures on the output light. The guided-mode resonance (GMR) concept refers to quasi-guided, or leaky, waveguide modes induced in periodic layers [24,25,26,27]. For the thermoelectric converter under study we adopt a simple thin film of p-type doped polysilicon that also furnishes the material for the integrated absorber. We focus our attention on the resonant absorption enhancement capability and omit actual fabrication of a corresponding thermopile; the principle provided can be applied in future complete devices and device arrays. We use rigorous coupled-wave analysis (RCWA) [28] to simulate the absorption spectra and compare them to unpatterned devices. Computed

results show that operating under GMR can enhance the absorption by ~30% for visible input light and ~40% in the IR range as compared to the performance of the unpatterned structure. The experimental results demonstrate that the integrated resonance segments can significantly enhance the electrical output relative to that of simple planar thermoelectric converters.

2.2 Design and Fabrication

We consider a resonance-coupled thermoelectric device as schematically depicted in Figure 2-2. The device includes a GMR absorber segment within the thermoelectric module and heavily doped p-type polysilicon as the functional material. A lot of thermoelectric materials were investigated in the past several decades and new materials are still, recently, being explored [29]. In this work we specifically selected p+ polysilicon for its high Seebeck coefficient and wide availability [30]. We aimed to demonstrate that GMR device can effectively enhance the light absorption thus improve the electrical output. Hence in the device design and experiments we emphasize material's Seebeck coefficient and the voltage output. We did not put much effort on the material's figure of merit and thus the device's efficiency. A ~2-μm-thick SiO_2 layer is adopted to enable GMR light absorption and to maintain a thermal gradient by blocking both light and heat leakage into the substrate. We deposit Al on both ends of the device to form ohmic contacts with the p+ polysilicon. When the input light radiation is absorbed and converted to heat a temperature difference will develop across the device as noted in Figure 2-2. Thereafter, the thermoelectric module converts the temperature difference across the device into electrical output by the Seebeck effect $\Delta V=S\Delta T$ in which ΔV is the voltage generated across the device, S is the Seebeck coefficient and, $\Delta T=T_H-T_L$ is the temperature difference.

Figure 2-3 shows the structure and parameters of the resonant absorber. We design two different absorbers working in the visible and IR wavelength ranges, respectively. We use RCWA to determine useful parameters. A measured doping concentration of ~$1\times10^{20}/cm^3$ for our p+ polysilicon film is obtained from resistivity measurement by using a standard four-point probe. The input wavelength is 0.4–0.9-μm for the "visible" range and 2–4-μm for the IR range. In the visible wavelength range, the complex refractive index n_c=n+jk of p+ polysilicon is approximately the same as that for undoped Si as shown in Fig. 9 and Fig. 10 in [31]. In the IR wavelength range the optical constants of p+ polysilicon are obtained from Fig. 4 in [32]. We can assume that the n and k values are approximately linear with wavelength within the 2–4-μm band. Figure 2-4 shows the n and k data we adopted in the simulation.

We establish values for the grating period (Λ), fill factor (F), and grating depth (d_g) to achieve high absorption. For visible light we obtain useful parameters as Λ = 0.7 μm, F = 0.4, d_g = 0.6 μm; for IR input we get Λ = 2 μm, F = 0.4, d_g = 0.8 μm. We use RCWA to simulate reflectance (R), transmittance (T) and absorptance (A) for devices with these parameters. Figure 2-5 shows the results for the visible range. It is evident that the resonance effects reduce light reflection and transmission thus increasing absorption. Figure 2-5 is for transverse-electric (TE) polarization in which the electric field vector of the input light is parallel to the grating lines. There exist no higher-order propagating diffracted waves as the device operates in the subwavelength regime.

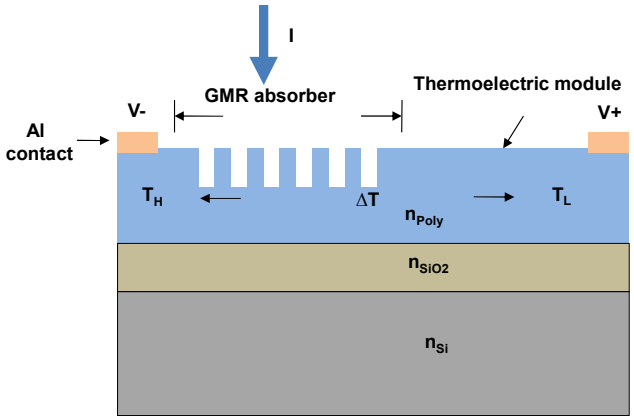

Figure 2-2 Schematic diagram of a resonant thermoelectric device. The device structure includes the absorber, thermoelectric converter, and Al contacts. Heavily p-type doped polysilicon is chosen as functional material. We assume normal incidence with visible light at λ = 0.4–0.9-μm or IR radiation at λ = 2–4-μm.

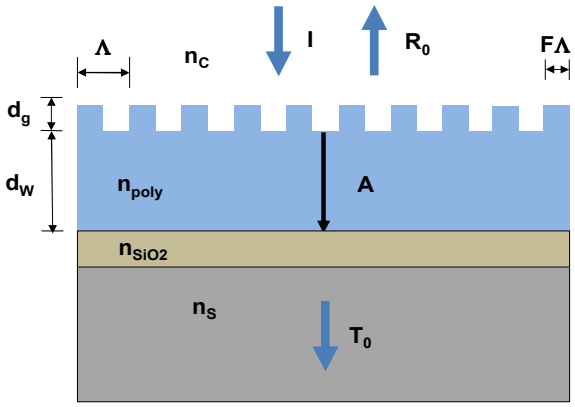

Figure 2-3 Schematic diagram of a GMR absorber denoting thicknesses (d) of the layers and refractive indices (n) of the various regions as well as the period (Λ) and fill factor (F) of the grating. We treat a periodic p+ polysilicon surface-relief boundary illuminated at normal incidence as shown.

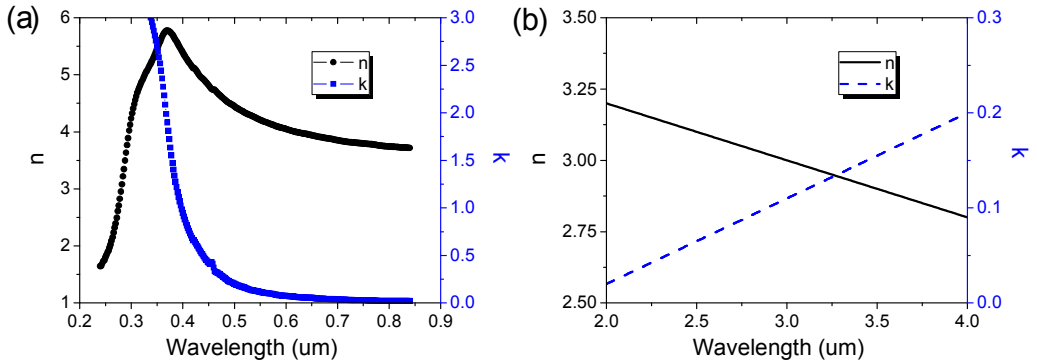

Figure 2-4 Optical constants n, k adopted for (a) visible region and (b) IR region devices.

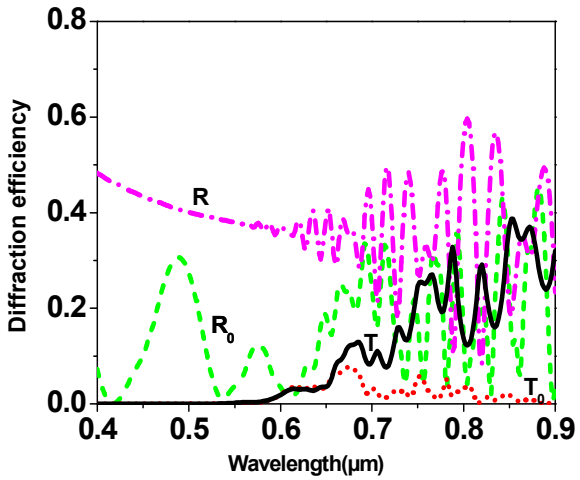

Figure 2-5 Computed zero-order reflectance (R_0) and transmittance (T_0) for a resonant device and corresponding R and T for an unpatterned device. The device parameters are Λ = 0.7 μm, F = 0.4, d_g = 0.6 μm, d_w =1.6 μm. The unpatterned device has no grating structure but only a 2.2-μm-thick flat polysilicon film.

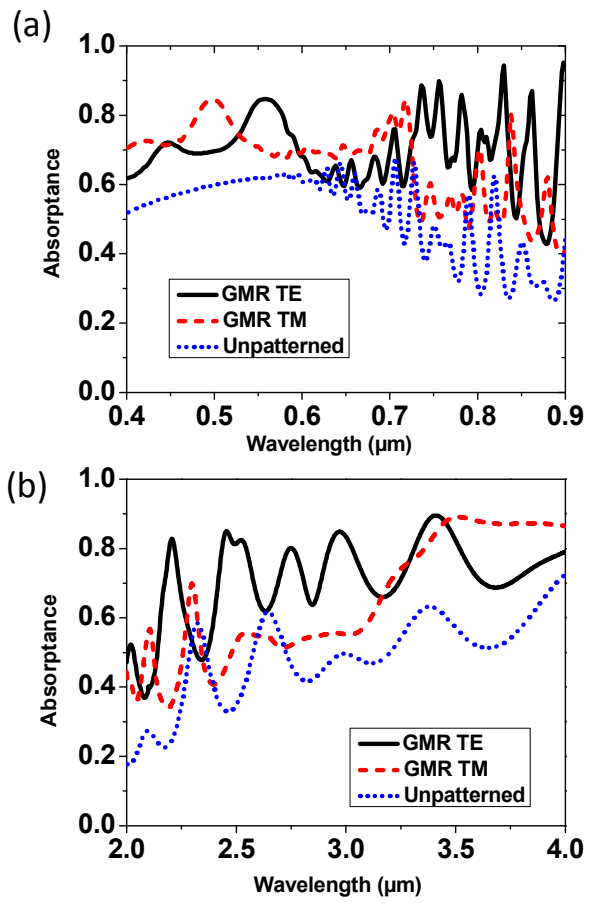

Figure 2-6 RCWA simulation of absorptance for resonant and unpatterned devices for both transverse-electric (TE) and transverse-magnetic (TM) polarization. (a) Visible region GMR device parameters are Λ = 0.7 μm, F = 0.4, d_g = 0.6 μm, d_w =1.6 μm; (b) IR region GMR device parameters are Λ = 2 μm, F = 0.4, d_g = 0.8 μm. The unpatterned device is a flat ~2.2-μm-thick polysilicon film.

Figure 2-6 shows results of simulating light absorption for visible and IR devices under TE and TM polarization. Averaging the response for TE- and TM-polarized input approximates the response for unpolarized light input. From Figure 2-6 we estimate that resonance operation enhances the integrated absorption by ~30% for visible light and ~40% for IR input as compared to the unpatterned device over the specified wavelength

range. For the IR devices we also simulate integrated absorption for Λ = 1 μm and Λ = 3 μm and obtain ~15% and ~30% enhancement ratio, respectively. Table 2-1 shows the simulation data for the integrated absorption enhancement for IR devices.

Table 2-1 Absorption enhancement for IR devices at various periods

Λ=1μm	TE	TM
Unpatterned	0.97	0.97
GMR	1.15	1.08
GMR Enhancement	19%	11%
Avg	15%	
Λ=2μm	TE	TM
Unpatterned	0.97	0.97
GMR	1.43	1.30
GMR Enhancement	47%	34%
Avg	41%	
Λ=3μm	TE	TM
Unpatterned	0.97	0.97
GMR	1.32	1.2
GMR Enhancement	36%	23%
Avg	30%	

Figure 2-7 shows the absorption under a small incidence angle variation for TE polarization. It is evident that the absorption curves within the whole wavelength range of interest are not affected much by the small incidence angle variation. We can obtain

similar results for TM polarization (results not shown). This is favorable for the experiments because it is allowed to keep not exactly normal incidence which is not practical in real experiments.

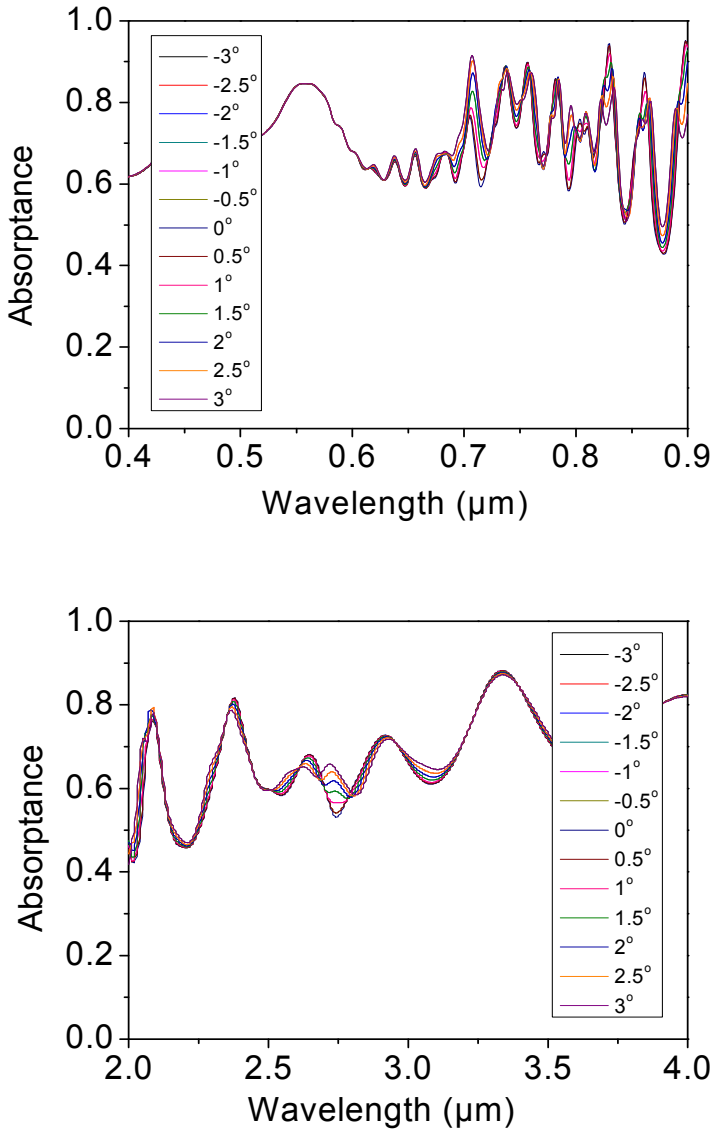

Figure 2-7 RCWA simulation of absorption under small variation of incidence angle for both visible and IR devices. TE polarization is assumed.

Figure 2-8 summarizes the fabrication steps. We start the device from a 4-inch p-type (100) silicon substrate. A ~2-μm-thick SiO_2 layer is grown on the substrate by wet thermal oxidation. Then a ~2.2-μm-thick polysilicon layer is deposited on the SiO_2 layer along with in-situ heavy doping of Boron. Thereafter, ~100-nm-thick bottom anti-reflection coating (BARC) layer and ~500-nm-thick positive photoresist (PR) layer are spun on the polysilicon layer at 1100- and 500 rpm, respectively. The BARC is baked at 205°C for 60 seconds and the PR is baked at 110ºC for 90 seconds. Then we use UV-laser interference lithography at 266 nm to obtain the PR pattern needed for the etching process. The exposed PR is developed for 60 seconds in AZ 917 MIF developer and rinsed with deionized water for 120 seconds. To pattern the polysilicon film we use reactive-ion etching (RIE) involving a gas mixture of CHF_3 and SF_6 to generate the polysilicon grating with the profiles used in the design step. After RIE, we strip the remaining PR and BARC grating using O_2 plasma. Finally, we deposit Al contacts with plasma sputtering.

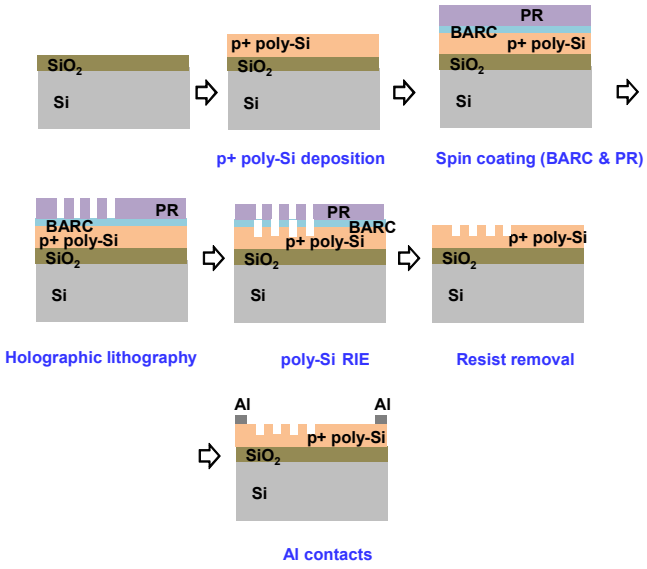

Figure 2-8 Process for fabricating resonant thermoelectric devices.

As stated above, we fabricate the devices to operate in visible light and at IR wavelengths. We characterize them using an atomic force microscope (AFM). From the AFM image and profile shown in Figure 2-9, we find that for the visible-region devices the key parameters are period $\Lambda \approx 0.69$ μm., fill factor $F \approx 0.4$, and grating depth $d_g \approx 0.59$ μm. For the IR devices we find period $\Lambda \approx 2$ μm, fill factor $F \approx 0.45$, and grating depth $d_g \approx 0.8$ μm. These parameters are all close to the design values. Figure 2-10 demonstrates the fabricated prototype devices which include three GMR devices and one unpatterned device.

2.3 Results and Discussion

To measure the electrical output and temperature differences we set up a test environment which included a light source (sun or IR source), lens, thermometer and voltmeter. We used actual sunlight as the input light source for the visible devices and an IR lamp for the IR devices (quartz tungsten halogen lamp). The lamp spectrum shows a broad irradiation range while containing the 2–4-μm wavelength range of interest here. During the test we put the samples directly under the lens to obtain focused light radiation. We then used the voltmeter to measure the electrical output and a thermometer to measure the temperature differences. Figure 2-11 shows the measurement setup for both visible and IR devices.

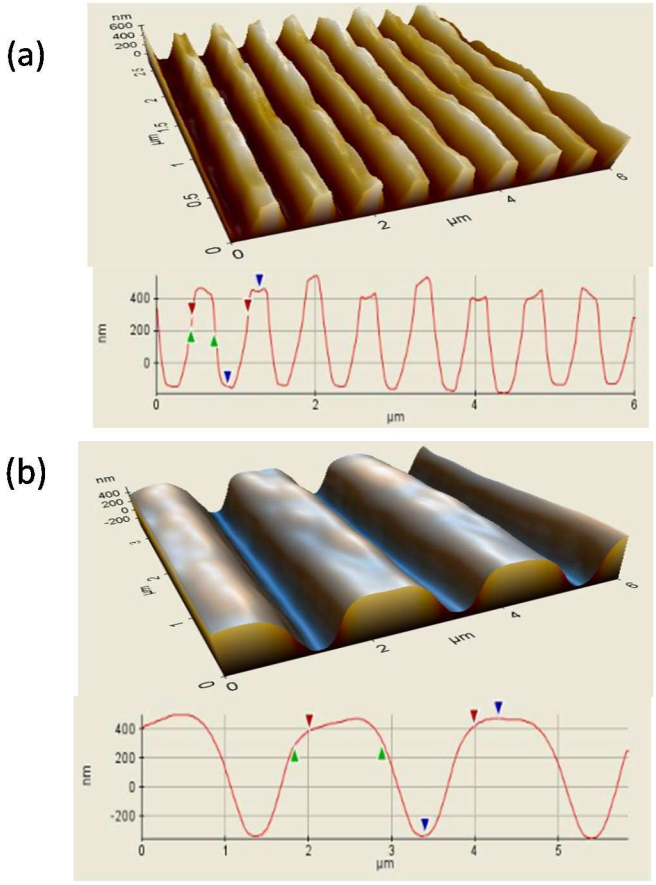

Figure 2-9 AFM images of the fabricated polysilicon gratings. For (a) the visible devices the parameters are $\Lambda \approx 0.69$ µm, F ≈ 0.4, $d_g \approx 0.59$ µm; for (b) the IR devices the parameters are $\Lambda \approx 2$ µm, F ≈ 0.45, $d_g \approx 0.8$ µm.

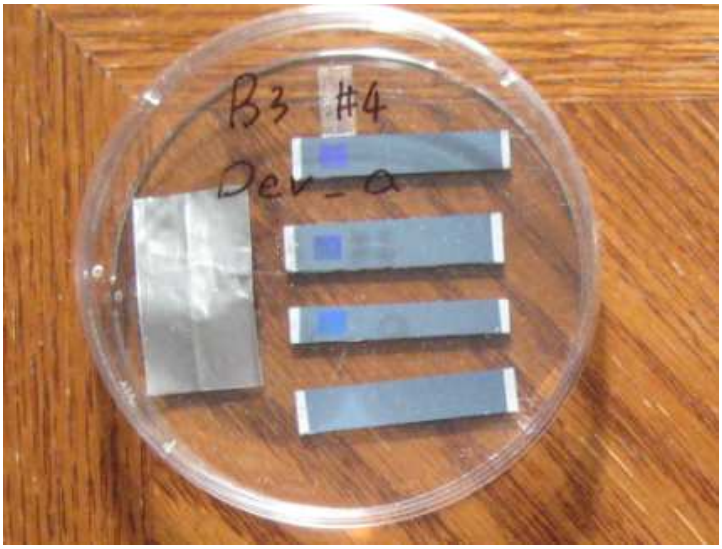

Figure 2-10 Fabricated prototype devices.

We fabricate arrays of prototype devices and perform statistical measurements as there is some inherent variability in the devices after processing and in the quality of the contacts. In the statistics we focus our attention on voltage output to demonstrate and quantify the resonance enhancement. Tables 2-2 and 2-3 show typical test results. For the visible region, the GMR devices are fabricated based on maximum absorption around Λ = 0.7 μm, F = 0.4, d_g = 0.6 μm. To prove that the resonance segments indeed enhance the electric output we compare to devices with randomly-patterned and unpatterned devices. From Table I we see that several GMR devices successfully demonstrate significant electrical output enhancement compared to the reference devices. Taking the statistical average of the Seebeck voltage, the GMR devices yield ~1.55 mV output whereas the randomly-patterned and unpatterned devices obtain ~0.77 mV and ~0.73 mV, respectively.

(a)

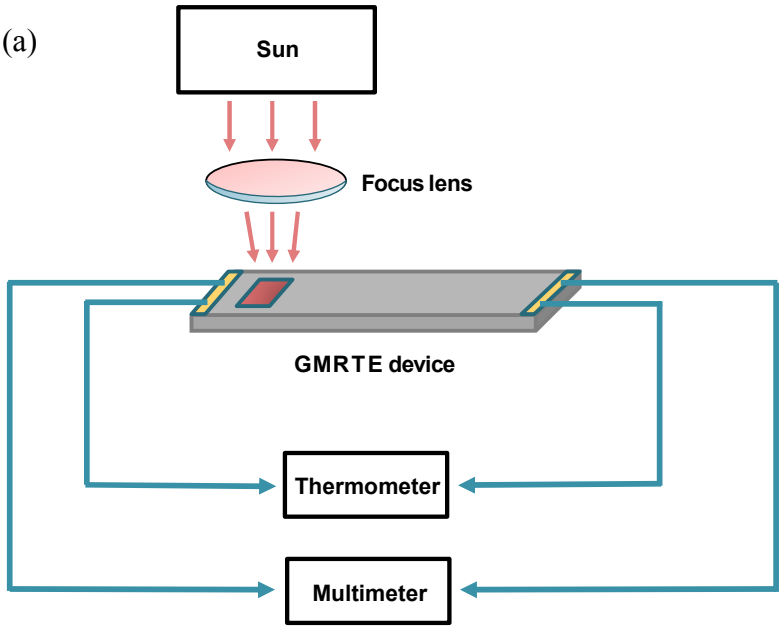

(b)

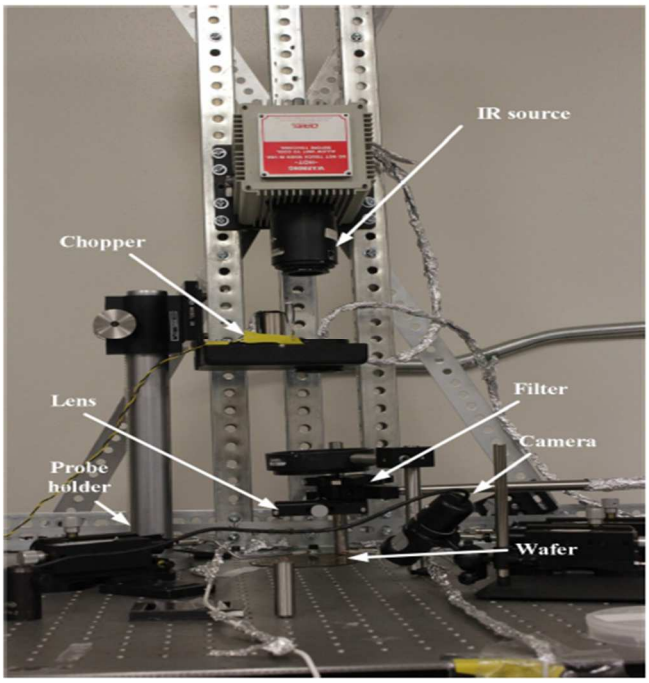

Figure 2-11 Measurement setup for the (a) visible (b) IR devices

Table 2-2 Electrical output measurement data for visible devices

Condition: Stable and focused sun, close to normal incidence GMR: Λ ≈ 0.69 μm, F ≈ 0.4, dg ≈ 0.59 μm Random: Roughened surface Unpatterned: Simple poly-Si slab				
Device	V (mV)	I (μA)	ΔT (°C)	V Average (mV)
GMR #1	1.6	0.5	5	1.55
GMR #2	1.5	0.4	5	
GMR #3	1.4	0.4	4	
Random #1	0.8	0.3	3	0.77
Random #2	0.8	0.2	3	
Random #3	0.7	0.3	3	
Unpatterned #1	0.8	0.3	4	0.73
Unpatterned #2	0.8	0.3	3	
Unpatterned #3	0.6	0.2	3	

Additionally, we test the IR-range devices to further demonstrate parametric impact. On the same wafer, we fabricate arrays of devices with absorbing patches fashioned with different periods Λ=1 μm, Λ=2 μm and Λ=3 μm. We compare the electrical output to that of unpatterned devices. For Λ=2 μm, the average voltage output is 10.5 μV, whereas for Λ=1 μm and Λ=3 μm devices the average output is ~1.75 μV and ~4 μV while the unpatterned devices yield ~1 μV. Thus, under the same test conditions, the 2-μm-period devices show the strongest enhancement. The reason for this is that the 2-μm-period induces the strongest light coupling and attendant mode concentration. Due to the low intensity of the available IR source, the temperature difference is very small and we cannot make precise measurements.

Table 2-3 Electrical output measurement data for IR devices

Condition: Focused QTH lamp, stable, normal incidence F ≈ 0.45, d_g ≈ 0.8 μm for all periods of GMR devices Unpatterned: Poly-Si slab		
Device	V (μV)	Average (μV)
GMR Λ=1μm	2	1.75
GMR Λ=1μm	1.5	
GMR Λ=2μm	11	10.5
GMR Λ=2μm	10	
GMR Λ=3μm	5	4
GMR Λ=3μm	3	
Unpatterned #1	1	1
Unpatterned #2	1	

2.4 Conclusion

In this chapter, prototype thermoelectric devices incorporating resonant absorbers were presented. They were compared to unpatterned and random-surface devices to verify performance enhancement. Simulation results show that the integrated resonant segments enhance the performance appreciably compared to the reference devices for both device classes tested. Additional research is needed to develop this concept further and optimize the design and fabrication for improved electrical output. These resonance-enhanced thermoelectric elements are simple and compact and may be useful in thermopile systems and as voltage generators or IR sensors.

Chapter 3

Guided-mode Resonant Mode – Competing Multiline Laser

3.1 Introduction

RESONANCE effects of various origins constitute the basis for photonic device engineering in a broad context. With roots in traditional diffractive optics, the guided-mode resonance (GMR) effect has been known for several decades [33,34,35]. Various models and numerical methods have been developed to analyze and understand pertinent device embodiments [36,37]. Based on numerical models, resonant structures have been designed with applications including lasers [38,39,40,41], optical filters [42], and resonant biosensors [43]. GMR-based mirrors can be viewed as being complementary to traditional thin-film dielectric mirrors. The GMR design has attributes not available in homogeneous thin films. In particular, in laser cavities, these mirrors directly polarize the output light and establish the laser's wavelength at the GMR resonance wavelength. In this chapter, we apply multiline GMR mirrors that support multiple simultaneous resonances to implement a multi-wavelength external cavity laser.

A recent study furnished a quantitative evaluation of the resonance properties of very thick resonance elements [44]. Accordingly, here we employ a thick glass waveguide grating that can support thousands of modes in the near-infrared spectral domain. The resulting filter possesses a dense population of resonant states with relatively narrow resonance bandwidths of individual spectral lines. We design a resonant reflector using rigorous coupled-wave analysis (RCWA). We fabricate the multiline mirror and apply it to an electrically pumped gain medium. We achieve selective laser lines that correspond to the dense resonance peaks generated by the mirror.

3.2 Design

We consider a TiO_2 grating on a glass membrane substrate as schematically depicted in Figure 3-1. Both the shallow grating and thick glass film function as a guided-mode resonator to produce a spectrally dense set of modes in the wavelength range of interest. This yields a dense resonance spectrum as shown in Figure 3-2.

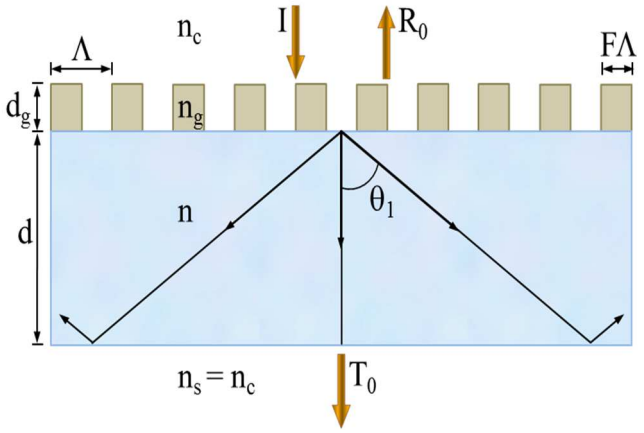

Figure 3-1 Schematic diagram of a multiline GMR filter denoting thicknesses (d) of the layers and refractive indices (n) of the various regions as well as the period (Λ) and fill factor (F) of the grating. We treat a thick glass slab with a periodic TiO_2 surface-relief boundary illuminated at normal incidence as shown. The period is chosen to be sufficiently small such that only the zero-order transmitted (T_0) and reflected (R_0) waves propagate in the air region.

For the present investigation, we select the 835- to 845-nm wavelength range that matches the amplifying spectral range of the gain chip. We specify a 700-nm period to allow only the first diffraction orders to exist in the thick waveguide. We select the fill factor (F = 0.4) and grating depth (d_g = 100 nm) to obtain reasonable bandwidths and spectral shape. To support a relatively high spectral density within this wavelength range, we set the waveguide thickness d to be 170 μm. Figure 3-2 shows the simulation and

experimental results of the reflectance (R_0) spectrum of the GMR multiline device. The experimental spectrum in Figure 3-2 (b) is obtained using a collimated broadband source (SuperK compact, Koheras) covering the spectral band from 500 nm to 2400 nm and a near-infrared spectrometer (HR4000, Ocean Optics) operating at a resolution of 0.1 nm.

The two spectral profiles show good agreement with each other in the spectral density of ~1.1 resonance modes/nm. The thickness of the device is the primary determinant of the spectral mode separation; thus a thinner glass slab will increase the separation and reduce the mode density. The observed degradation of the resonance contrast in the experimental spectrum is due to non-zero divergence of the incident light in the experiment. In contrast to the theoretical calculation in Figure 3-2 (a), the experimental spectrum in Figure 3-2 (b) shows a reflection peak split by 0.23 nm. This peak splitting is induced by slightly off-normal light incidence with the angle of incidence $\theta \approx 0.2°$. In addition, non-zero divergence of the incident light results in additional peak broadening and resonance contrast degradation as explained in [35]. As the laser locks onto the resonance peaks, this reduced reflectance suffices to attain lasing as demonstrated herein.

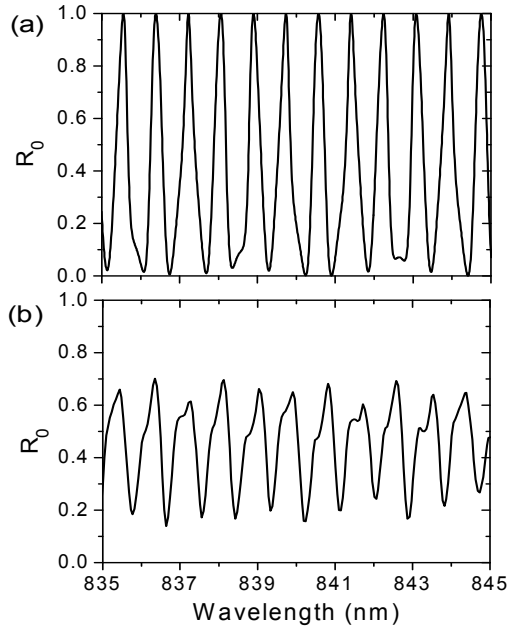

Figure 3-2 Calculated (a) and measured (b) reflectance (R_0) spectra of the multiline GMR device. Transverse-electric (TE) polarization, with the electric vector normal to the plane of incidence, is assumed for the incident light. Simulation parameters of the multiline GMR device are Λ = 700 nm, F = 0.4, and d_g = 100 nm. Measured device parameters are Λ = 700 nm, F = 0.39, d_g = 107 nm, n_s=1, n_g=2.5, and n=1.52.

3.3 Fabrication and Characterization

Figure 3-3 summarizes the fabrication steps. We use a 40 $\times$ 24 mm^2 glass membrane with a ~170-μm thickness. A ~100-nm-thick TiO_2 layer is deposited on the top of the membrane to form the grating layer. We establish the refractive index of the TiO_2 film as 2.5 based on ellipsometric measurements. Thereafter, a 300-nm-thick positive photoresist (PR) layer is spun on the TiO_2 layer at 1200 rpm. The PR is baked at 110ºC for 90 seconds. Then we use UV-laser interference lithography at 266 nm to obtain the PR pattern needed for the etching process. The exposed PR is developed for 60 seconds

in AZ 917 MIF developer and then rinsed with deionized water for 120 seconds. To pattern the TiO_2 film, we use reactive-ion etching (RIE) involving a gas mixture of CHF3 and CF4 to generate the TiO_2 grating with the profiles used in the design step. After RIE, we strip the remaining PR grating using O_2 plasma.

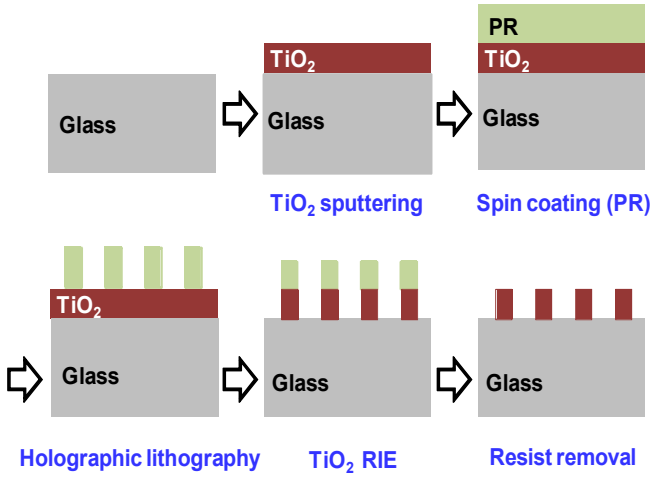

Figure 3-3 Multiline GMR laser mirror fabrication steps.

We characterize the device using an atomic force microscope (AFM). From the AFM image and profile shown in Figure 3-4, we verify that the parameters, period Λ = 700 nm, fill factor F = 0.39, and grating depth d_g = 107 nm, are close to the design values.

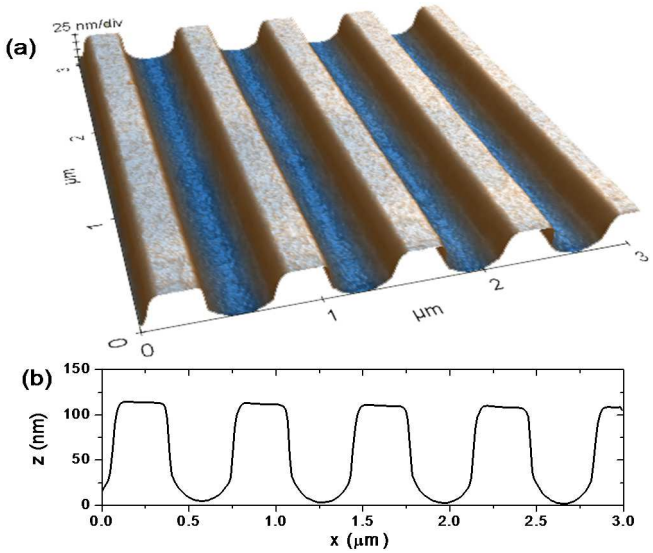

Figure 3-4 AFM image (a) and profile (b) of the fabricated TiO_2 grating; the device parameters are Λ = 700 nm, F = 0.39, and d_g = 107 nm.

3.4 Results and Discussion

We apply the multiline device with a gain chip to measure the output spectrum. The gain chip is an electrically pumped laser diode with a GaAlAs/GaAs quantum well (QW) and a thin waveguide layer that possesses a gain bandwidth range spanning 820-850 nm. The gain chip is electrically pumped with a precision current source (ILX Lightwave LDX-3412), and its temperature is kept constant with a temperature controller. Figure 3-5 shows the laser measurement setup. A near-infrared spectrometer (HR4000, Ocean Optics) operating at a resolution of 0.1 nm is used to gather the spectral data of the output signal.

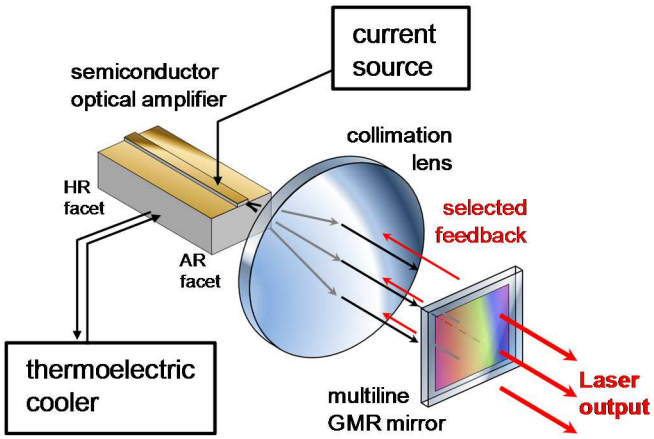

Figure 3-5 Wavelength-selective external cavity laser output measurement setup.

Figure 3-6 shows the measured gain spectrum with (blue) and without (red) GMR device feedback. The transmission spectrum shows comb-like multi-resonance peaks within the gain chip's emission bandwidth spanning 830-850 nm. The experimental spectra show reasonable agreement with the simulated spectra in the number of resonance peaks per spectral interval.

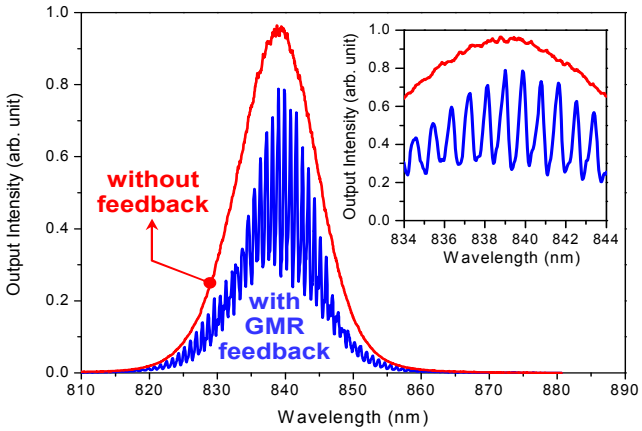

Figure 3-6 Measured gain spectrum with (blue) and without (red) GMR device feedback. Device parameters are Λ = 700 nm, F = 0.39, and d_g = 107 nm. The injection current is ~40 mA for this measurement.

Increasing the gain chip's injection current to provide sufficient optical gain above the lasing threshold establishes the laser oscillation of the multi-resonance lines. Figure 3-7 shows the output spectra at an injection current of 100 mA. This injection current value provides optical gain well beyond the lasing threshold for the GMR lines in the wavelength range of 834-846 nm. In Figure 3-7(a), four lasing lines oscillate at 837.8 nm, 838.7 nm, 840.5 nm, and 842.3 nm. Since this mode is near its optimum, it realizes the maximum gain and suppresses the neighboring modes. By selecting a single mode in the series of lasing lines, specifically 840.5 nm, we obtain a stable laser oscillation as demonstrated in Figure 3-7(b). We obtain this mode selection by finely aligning the collimation lens with respect to the gain chip. Chromatic aberration causes spatially separated feedback focal spots to form along the collimation lens's optical axis. By tuning the working distance of the collimation lens, we select a focal spot that directs the dominant feedback to the gain chip when its optical waveguide aligns precisely with the collimation lens's optical axis. Note that we obtain the unstable multimode operation in Figure 3-7(a) when the chip's optical waveguide is off-axis relative to the collimation lens. The focal length of the collimation lens is ~5 mm; it can be finely adjusted to slightly change the tilt angle and position.

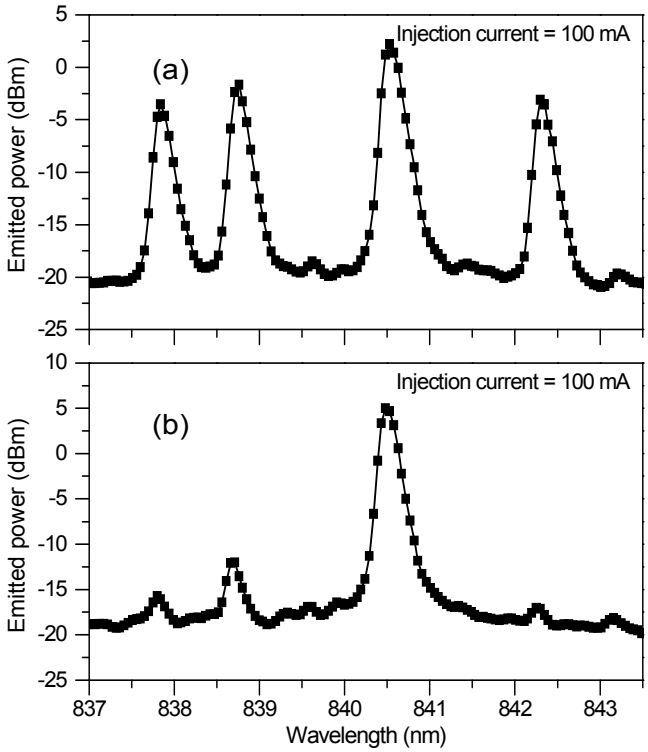

Figure 3-7 Measured hopping laser lines and an example stable single laser line. (a) Four laser lines competing for the gain simultaneously; (b) a stable single laser line achieved by fine tuning the laser mirror relative to the chip.

Figure 3-8 shows the measured stable laser lines and corresponding lasing characteristics at different mode wavelengths. Within the 835- to 845-nm wavelength range, the thick GMR devices have ~10 resonance peaks and every peak can generate a laser line. We select three typical peaks (left, middle, and right) to illustrate the lasing mode wavelength selectivity and its associated properties. Figure 3-8(a) shows the selected stable laser lines at 836.6 nm, 840.5 nm, and 843.7 nm where the linewidth is (FWHM) < 0.5 nm. This spectral width is defined by the linewidth of the GMR mirror. Figure 3-8(b) compares the emitted peak power to the injection current for the

corresponding laser lines in Figure 3-8(a). These three curves show typical nonlinear lasing characteristics with a threshold current of ~65 mA. Figure 3-9 shows every resonance peak can generate a corresponding stable laser line. As we stated in the description of Figure 3-7 a stable laser line can be achieved by finely adjusting the collimation lens to make one of the resonance peaks best aligned with the gain chip waveguide. So every resonance peak can generate a corresponding stable laser line when that resonance peak is best aligned to the waveguide by finely adjusting the collimation lens.

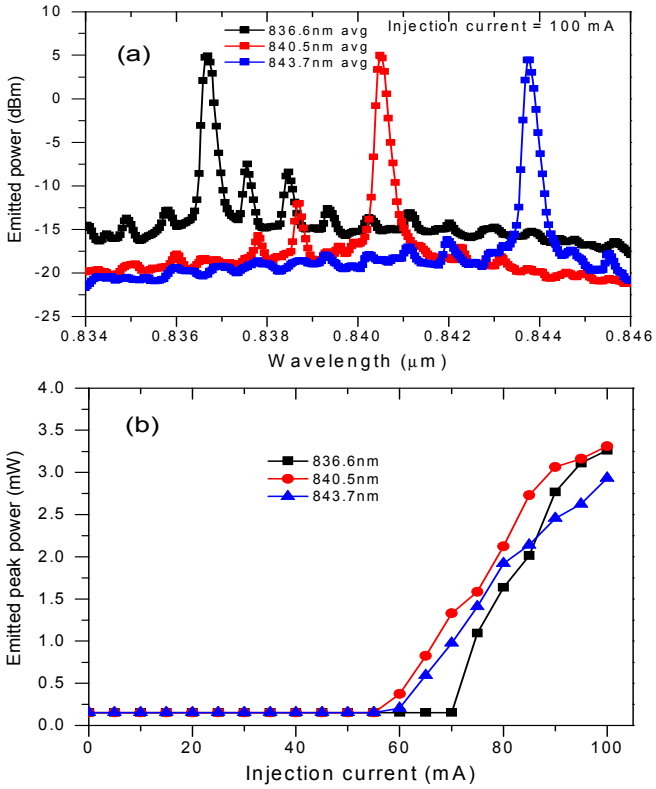

Figure 3-8 Measured selected stable laser lines and their lasing characteristics. Lasing wavelengths are 836.6 nm (black), 840.5 nm (red), and 843.7 nm (blue). (a) Three typical lines with different wavelengths measured at a 100-mA injection current. (b) Corresponding lasing characteristics.

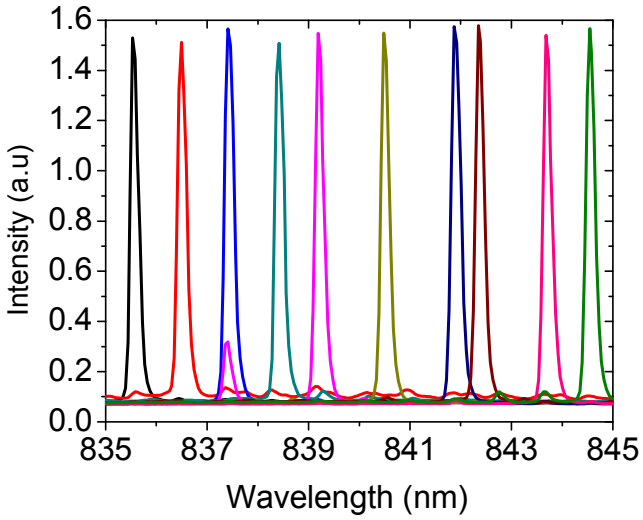

Figure 3-9 Stable laser lines generated by every resonance peak.

3.5 Conclusions

In this chapter, we demonstrated a wavelength-selective external cavity laser using a multiline GMR filter as the laser mirror. The experimental results demonstrate that a stable selective laser line can be generated from every resonance peak of the GMR multiline device. As reasonable agreement is found between the multiline device's generated laser lines and their corresponding resonance peaks, these preliminary results verify the applicability of multiline GMR devices. Investigation of analogous resonance structures using other material systems and spectral regions may extend the application potential of this device class.

Chapter 4

Dense-Grid Multiline Photonic Filters: Theory and Experiments

4.1 Introduction

In photonic device engineering, resonance effects of various origins can be applied to sculpt versatile spectra. Often a single resonance in a given spectral band is sufficient to design useful devices. For example, a guided-mode resonance biosensor employing a single resonance can indicate whether or not a particular bioreaction occurs [45]. In contrast, multichannel filters passing or blocking selected sets of wavelengths are of interest as arrayed waveguide gratings in telecommunication systems [46]. Whereas periodic resonance elements supporting a single, or a few, resonance lines have been widely studied in nanophotonics and nanoplasmonics, while much less effort has involved multiline devices.

Generation and application of multiline spectra is presently of great scientific interest. To this end, various and conceptually diverse means can be employed. For example, generation of optical frequency combs in microresonators supporting whispering-gallery modes while engaging nonlinear optical effects is important for a host of potential applications [47]. A totally different approach for comb generation applies a pair of chirped Bragg gratings in a silicon-chip layout geometry [48]. A comb-filter concept engaging a gas-filled photonic crystal fiber with a heating implement for modal interference has been proposed [49]. A tunable multiline comb filter including Sagnac loops and periodic interleaved p-n junctions has been shown to be feasible [50]. In this paper we propose a new type of multiline filter based on guided-mode resonance effect. Originated in traditional diffractive optics, the guided-mode resonance (GMR) effect has been researched over several decades [51,52,53,54]. GMRs occur due to quasi-guided, or leaky, waveguide modes that can be induced on patterned films. Nanopatterns with

subwavelength periods yield the highest resonance efficiencies, as non-zero-order diffracted waves carry no power. Various models and numerical methods such as rigorous coupled-wave analysis (RCWA) have been developed to understand and describe this optical phenomenon [54,55,56]. Based on theoretical research, numerous types of devices have been designed and fabricated with application to energy, information technology, and sensors. In particular, diverse species of optical filters that employ the GMR effect have been investigated including reflection filters, transmission filters, and Brewster filters [57].

Recently, by theoretical methods, we analyzed the feasibility of comb-like multiline GMR filters that operate with an extremely thick periodic waveguide layer [58]. This concept was subsequently applied to realize experimentally a multiline laser exhibiting several simultaneous resonant laser lines near the λ=840 nm wavelength [59]. Motivated by these results, the objective of this present work is to design and fabricate multiline GMR filters in different material systems and explore their potential applications. To achieve this goal, we employ thick waveguide layers such as silicon wafers or glass slides that can support thousands of modes. The resulting GMR comb-like filters possess a dense population of resonant states with relatively narrow resonance bandwidths of individual spectral lines being possible and controllable by design. We realize practical designs with well-shaped resonance spectra using RCWA. We fabricate the designed filters and compare experimental performance with theoretical predictions in the near infrared (NIR) spectral region at the telecommunication c-band.

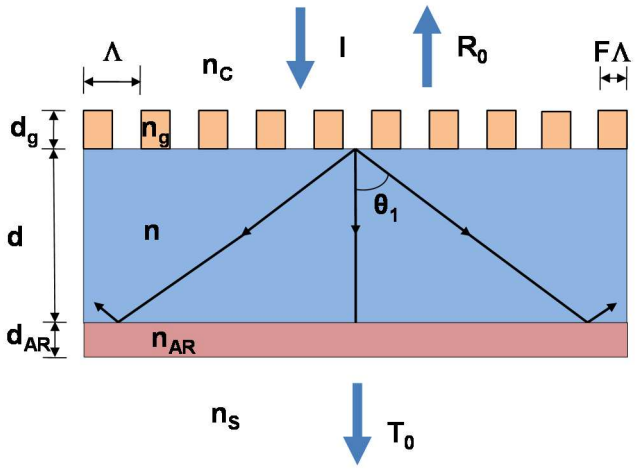

Figure 4-1 Schematic diagram of a multiline GMR filter denoting thicknesses (d) of the layers and refractive indices (n) of the various regions as well as the period (Λ) and fill factor (F) of the grating. We treat a thick silicon slab with a periodic boundary illuminated at normal incidence. We assume TE or TM-polarized input light with electric-field vector normal or parallel to the plane of incidence. The period is chosen to be sufficiently small such that only the zero-order transmitted (T_0) and reflected (R_0) waves propagate external to the device. A single-layer antireflection (AR) coating designed for normal incidence may be placed at the bottom surface.

4.2 Design and Simulation

4.2.1 One Dimensional Multiline GMR Device

1D multiline GMR devices are polarization dependent. Under the same design parameters the transverse-electric (TE) and transverse-magnetic (TM) spectra are significantly different. The design parameters are optimized for TE polarization. We consider a Si slab waveguide supporting a grating as depicted in Figure 4-1. The waveguide grating structure functions as a guided-mode resonator to produce a spectrally-dense set of guided-modes in the spectral band of interest. On the bottom of

the device, a thin antireflection (AR) layer can be deposited to eliminate the interference between the resonant diffraction orders and the reflection generated by the directly transmitted zero-order wave; this yields a well-shaped, low-sideband resonance spectrum as shown in [14].

In the first design, we select Si for both the waveguide and grating. We specify an 800 nm period to allow only the first diffraction orders to exist in the thick waveguide. Fill factor (F = 0.16) and grating depth (d_g = 190 nm) are selected to obtain narrow bandwidths and low sidebands. We set the AR layer thickness at d_{AR} = 0.208 μm and refractive index at n_{AR} = 1.865.

To demonstrate the peak density is determined by waveguide thickness, we set the waveguide thickness d to be 10, 30, 100, 300 μm, respectively. Figure 4-2 (a)-(d) shows the spectra for the TE-polarized filter; as per design the filter lines are well shaped and reach zero reflectance to define a channelized spectrum as illustrated in the figure. For d = 10, 30 μm thickness we set the wavelength range to be 1500-1600 nm; for d = 100, 300 μm thickness due to the large density of resonance peaks we limit our attention to the 1540-1560 nm wavelength range. Figure 4-3 (a)-(d) shows the TM spectrum generated by the same device; it is clearly not optimized. We can obtain similar spectra for TM as the optimized TE spectra in Figure 4-2 by further optimizing TM parameters. As simulation shows we can implement that by employing a fill factor value for TM which equals one minus the fill factor value of TE while keeping other design parameters unchanged. This can be well explained by the effective medium theory (EMT) which states that the effective index of the grating layer keeps the same if the fill factor of the grating for TE polarization equals one minus the fill factor of the grating for TM polarization.

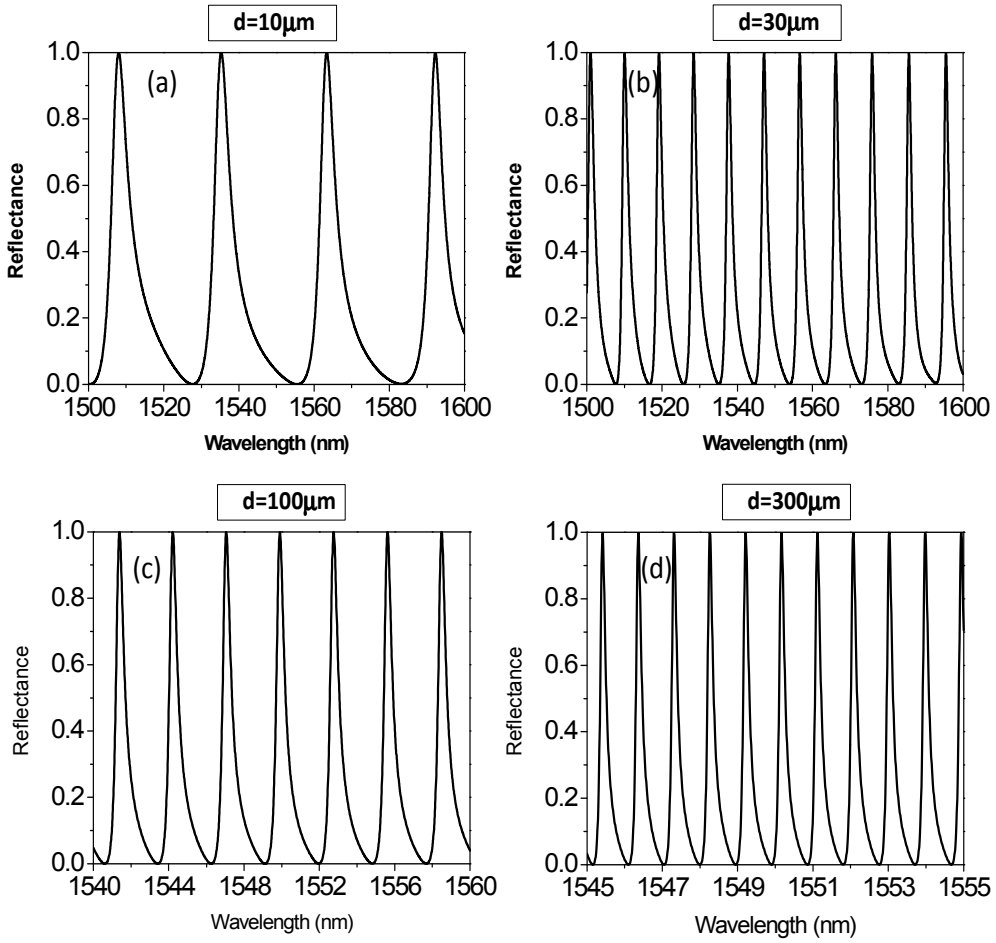

Figure 4-2 Calculated reflection spectra in TE-polarization applying a Si waveguide and Si grating design. The design parameters of the GMR filter are Λ = 800 nm, F = 0.16, d_g = 190 nm, n_g = 3.5, n = 3.5, n_{AR} = 1.865, and d_{AR} = 208 nm; d = 10, 30, 100, 300 μm respectively.

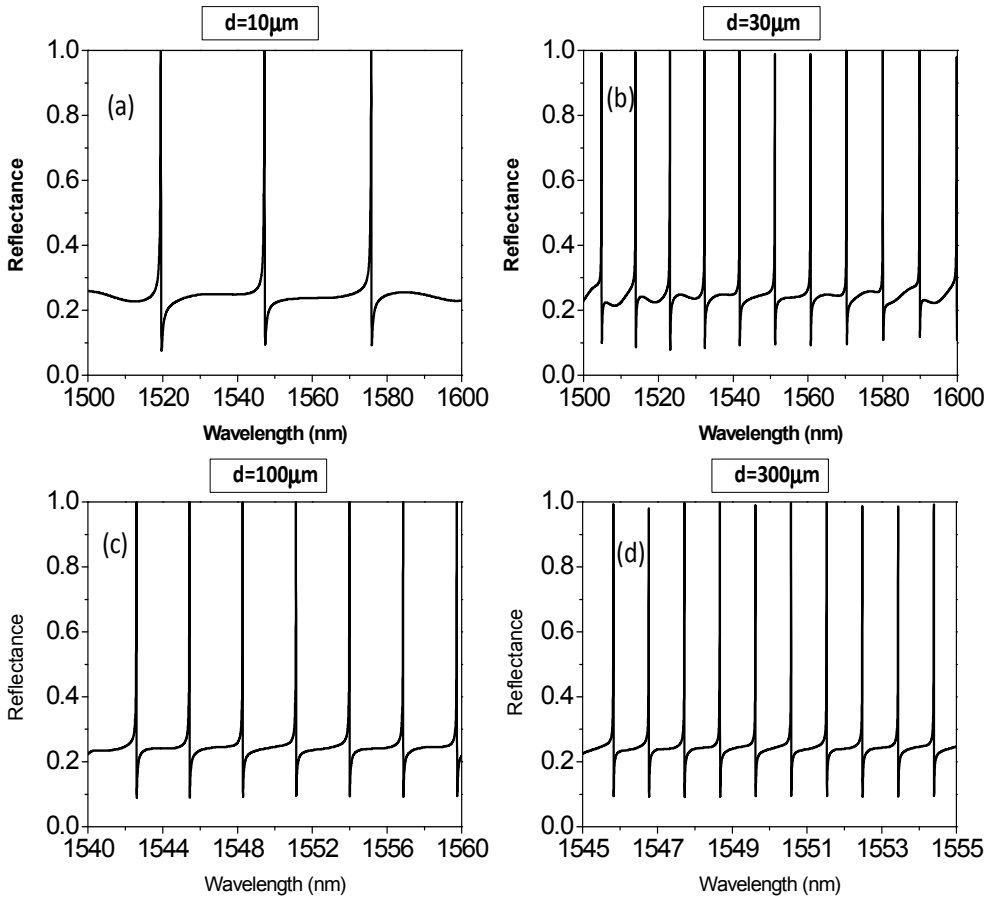

Figure 4-3 Calculated reflection spectra in TM-polarization applying a Si waveguide and Si grating design. The design parameters of the GMR filter are Λ = 800 nm, F = 0.16, d_g = 190 nm, n_g = 3.5, n = 3.5, n_{AR} = 1.865, and d_{AR} = 208 nm; d =10, 30, 100, 300 μm respectively.

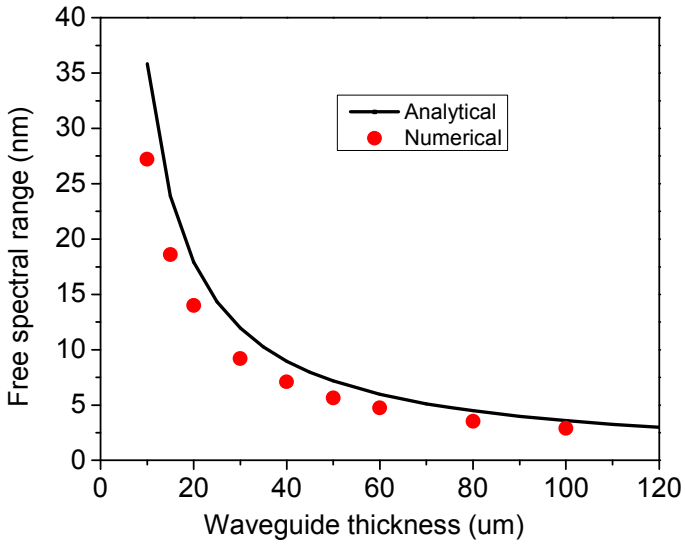

Figure 4-4 Analytical and simulation results of the relation of free spectral range with waveguide thickness.

Figure 4-4 shows the relation of free spectral range (FSR) with waveguide thickness around 1550nm wavelength. From the mode equation $M \sim (2d/\lambda)(n_f^2 - n_c^2)^{1/2}$ we can derive the analytical expression of free spectral range with waveguide thickness described as $FSR \cong \lambda^2/(2d)(n_f^2 - n_c^2)^{1/2}$,where M is mode number, d is waveguide thickness, λ is free space wavelength, n_f and n_c are the refractive index of waveguide and cover layers, respectively. We also simulate the relation using RCWA at several waveguide thicknesses. The error between analytical and numerical results is ($FSR_{ana} - FSR_{num}$) / FSR_{ana}, approximately 20%.

To further improve the filter's performance, in a second embodiment we employ TiO_2 for the grating while retaining the Si wafer slab waveguide. We limit our attention to the d = 300 μm thickness and 1545-1555 nm wavelength range. In the design phase, we arrive at a fill factor of F = 0.32 and grating depth of d_g = 204 nm whereby narrower

bandwidths and lower, flatter sidebands are attained as depicted in Figure 4-5(a). Other parameters remain the same as in the Si grating design in Figure 4-2 (d). Figure 4-5 (b) provides the corresponding reflectance spectra associated with TM-polarized incident light.

To connect with a familiar, classic resonator response, we also compute the corresponding Fabry-Perot (FP) resonance spectrum using the bare unpatterned Si wafer with results shown in Figure 4-6. Compared to the GMR spectra, the FP slab possesses a lower spectral density and reduced resonance contrast. The fundamental physical differences between these device concepts are clear. An FP resonator has a possibility of 100% transmission when $d = q\lambda/2n$, q being an integer. It has no such absolute conditions in reflection. In contrast, the thick GMR device has a possibility of 100% reflection when the round-trip phase is near $2\pi q$, i.e. a slab waveguide mode is excited.

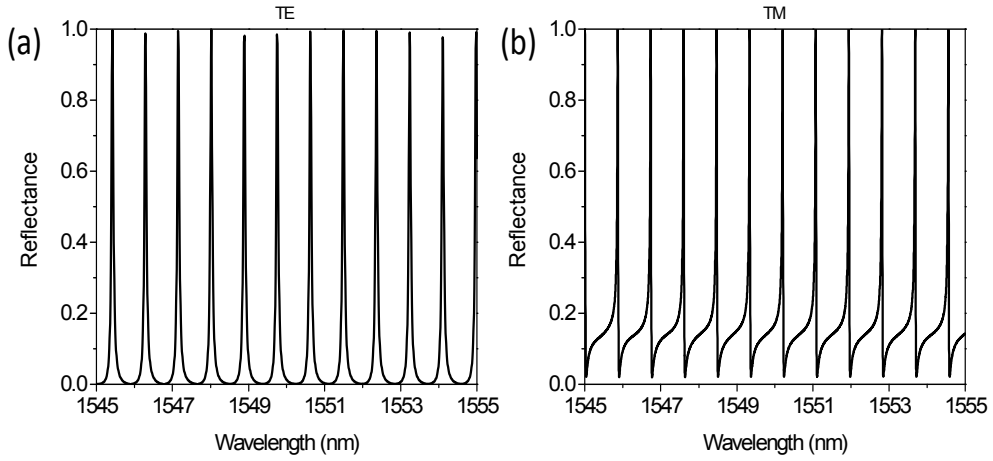

Figure 4-5 Calculated reflection spectra in (a) TE- and (b) TM-polarization using a Si waveguide and a TiO_2 grating design. The design parameters of the GMR filter are Λ = 800 nm, F = 0.32, d_g = 204 nm, d = 300 μm, n_g = 2.5, n = 3.5, n_{AR} = 1.865, and d_{AR} = 208 nm.

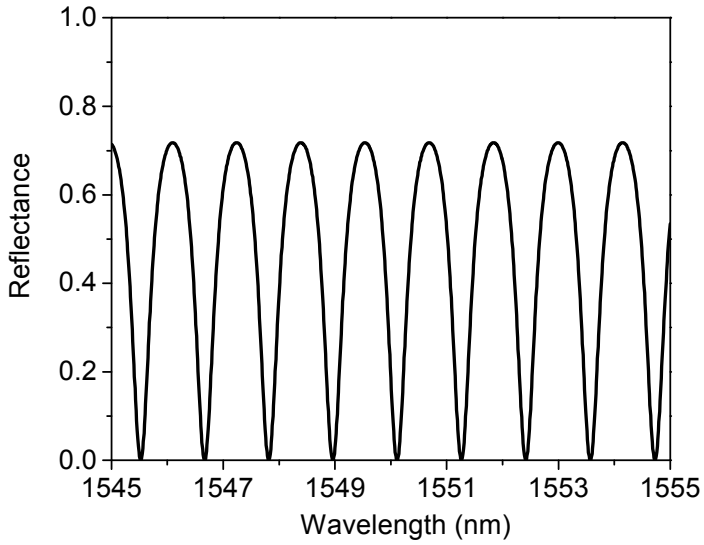

Figure 4-6 Calculated Fabry-Perot reflection spectrum associated with a Si slab illuminated by a normally-incident plane wave. The unpatterned slab is 300-μm thick and has no AR sublayer.

4.2.2 Polarization Independent Multiline GMR Device

We achieve polarization independent spectra by employing two dimensional (2D) GMR structure. The 2D structure is similar to 1D structure as shown in Figure 4-1 except that the gratings are distributed at both X and Y directions. Here we omit the schematic diagram. For the present investigation, we sample the 1548-1552 nm wavelength range. We note that similar effects prevail across much larger spectral bands for the devices presented. We specify a 600 nm period to allow only the first diffraction orders to exist in the thick waveguide. By design, the fill factor ($F_x = F_y = 0.5$) and grating depth (d_g = 190 nm) are established to obtain narrow bandwidths and low sidebands. To support a relatively high spectral density within this wavelength range, we set the waveguide thickness d to be ~300 μm. We set the AR layer thickness at d_{AR} = 208 nm and refractive

index at n_{AR} = 1.865. We compute both TE and TM polarization. Figure 4-7 shows the calculated spectra. Compared to 1D multiline spectra we note that there exists double peaks that are induced by both X and Y directions gratings. The sharper peaks are caused by the TM modes in the thick waveguide.

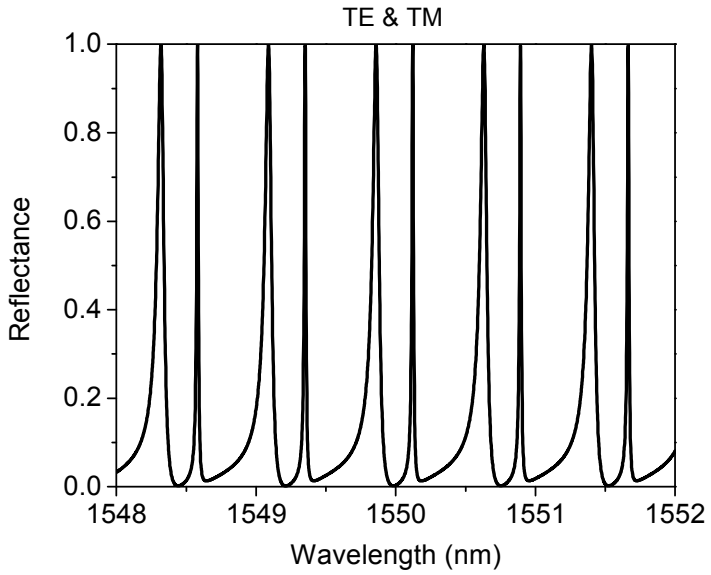

Figure 4-7 Calculated reflection spectra of the unpolarized light incidence. Device parameters of the 2D GMR filter are $\Lambda_x = \Lambda_y = 600$ nm, $F_x = F_y = 0.5$, $d_g = 190$ nm, d = 300 μm, $n_g = n = 3.48$, $n_{AR} = 1.865$, and $d_{AR} = 208$ nm.

Figure 4-8 calculates the modes that can be supported by the thick waveguide. Calculated wavelength range is 1.5-1.6 μm. V is the normalized frequency and thickness parameter, V= $\frac{\omega}{c} h \sqrt{n_f{}^2 - n_s{}^2}$; b = $\frac{N^2 - n_s{}^2}{n_f{}^2 - n_s{}^2}$; ω is the angular frequency, c is the free space light speed, h is the waveguide thickness, n_f is waveguide refractive index, n_s is the substrate index and N= $n_f \sin\theta$, θ is the mode angle. We can see that under the same b value, that is, the same mode angle, there simultaneously exists one TE mode and one

adjacent TM mode within the specified wavelength range corresponding to the double peaks shown in Figure 4-7. The modes distance can be calculated by data in Figure 4-8 and above V formula, and they are close to the double peaks distance value of 0.26 nm in Figure 4-7.

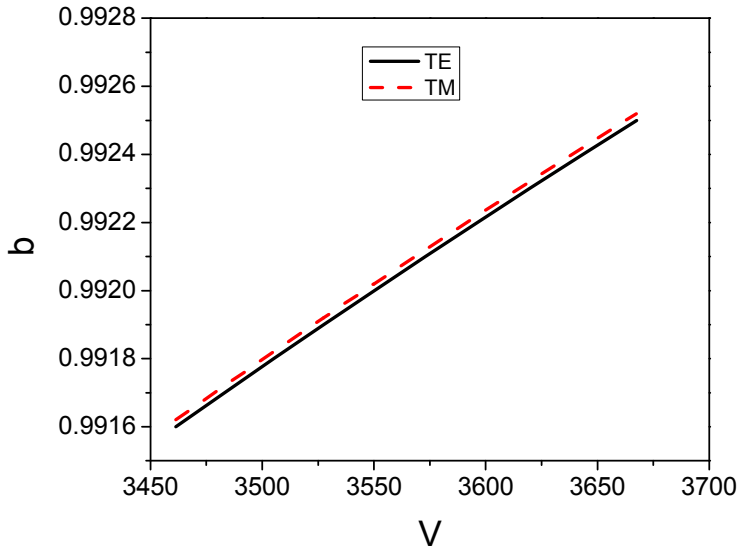

Figure 4-8 Calculated TE and TM modes that can be supported by thick waveguide within wavelength range of 1.5- 1.6 μm.

4.2.3 Brewster Multiline GMR Device

In 1D multiline device design we investigate another approach to obtain low sideband without anti-reflection (AR) layer. This can be realized by Brewster incidence under TM polarization. The Brewster device structure is similar to 1D structure in Figure 4-1 except that the incident light is at TM polarization and Brewster angle. Meanwhile AR layer is not needed. Figure 4-9 shows the Brewster filter configuration.

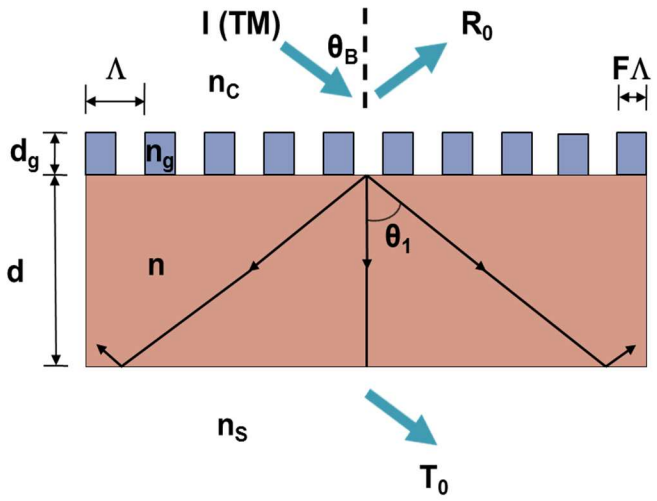

Figure 4-9 GMR Brewster multiline filter configuration

For the present investigation, we limit our attention to the 1540-1560 nm wavelength range. We note that similar effects prevail across much larger spectral bands for the devices presented. We simulate the angular response within NIR wavelength range to find the Brewster angle for quartz slab to be ~56°. In Figure 4-10 we simulate the multiline spectrum under Brewster incidence for a practical design. The design parameters are Λ = 800 nm, F = 0.5, d_g = 160 nm, d = 170 μm, n_g = n = 1.5. From the figure we can see that extremely narrow FWHM of ~0.02 nm and very flat, low sideband of ~10^{-3} can be achieved.

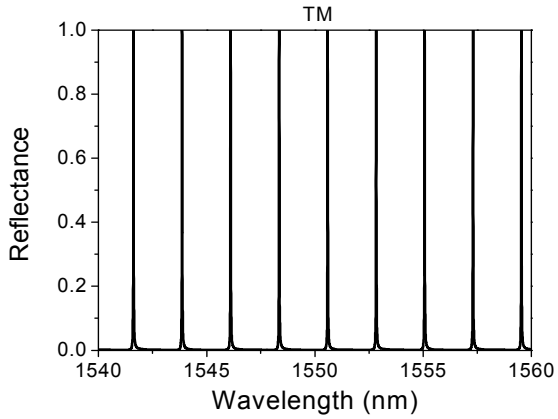

Figure 4-10 Simulated Brewster multiline device spectrum. Device parameters are Λ = 800 nm, F = 0.5, d_g = 160 nm, d = 170 μm, n_g = n = 1.5.

4.3 Fabrication and Characterization

Here we present a typical 1D multiline GMR device fabrication steps with Si waveguide and TiO_2 grating. The 2D steps are similar to 1D case except that 2D case needs exposure on both X and Y directions. We start the filter fabrication on a 2-inch double-side-polished Si wafer with a ~300 μm thickness. Figure 4-11 summarizes the detailed fabrication steps. A ~200-nm-thick TiO_2 and Si_3N_4 layers are deposited on the top and bottom sides of the Si wafer, respectively, to form the grating and AR layers. The refractive index of TiO_2 and Si_3N_4 are measured by ellipsometry to be 2.5 and 1.93, respectively. Thereafter, a 300-nm-thick positive photoresist (PR) layer is spun on the TiO_2 layer at 1200 rpm. The PR is baked at 110ºC for 90 seconds. Then we use UV-laser interference lithography at 266 nm to obtain the PR pattern needed for the etching process. The exposed PR is developed for 60 seconds in AZ 917 MIF developer and then rinsed with deionized water for 120 seconds. To pattern the TiO_2 film, we use reactive-ion etching (RIE) involving a gas mixture of CHF_3 and CF_4 to generate the TiO_2

grating with the profile used in the design step. After RIE, we strip the remaining PR grating using O_2 plasma.

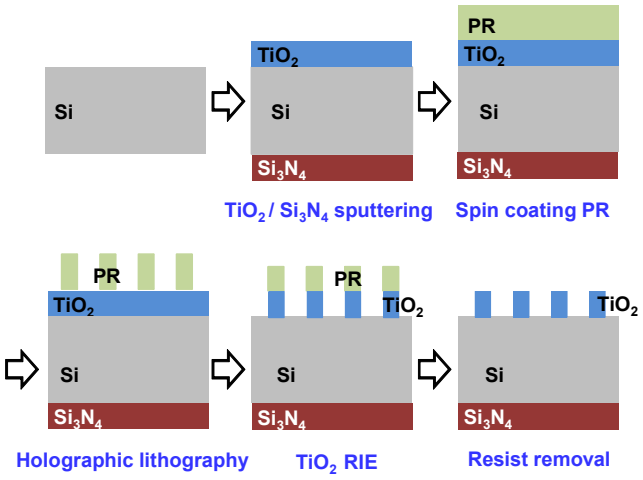

Figure 4-11 Main steps in the fabrication of GMR multiline filters.

The Si grating device is characterized using an atomic force microscope (AFM). From the AFM image and profile in Figure 4-12 we verify the period, grating depth, and fill factor. The AFM profile in Figure 4-12 (b) yields Λ = 798 nm, F = 0.17, and d_g = 193 nm; these parameters are close to the design values. Another similar device is also characterized by AFM and Λ = 800 nm, F = 0.2, and d_g = 195 nm are obtained.

The TiO_2 grating device is characterized with an atomic force microscope (AFM). From the AFM image and profile in Figure 4-13, we verify the period, grating depth, and fill factor. The AFM profile in Figure 4-13 (b) yields Λ = 800 nm, F = 0.36, and d_g = 209 nm; these parameters are close to the design values.

We also fabricate some 2D devices. The device is characterized with an atomic force microscope (AFM) and scanning electron microscope (SEM). From the AFM and SEM image and profile in Figure 4-14, we verify the period, grating depth, and fill factor. The AFM profile yields Λ = 800 nm, $F_x = F_y$ = 0.3, d_g = 190 nm;

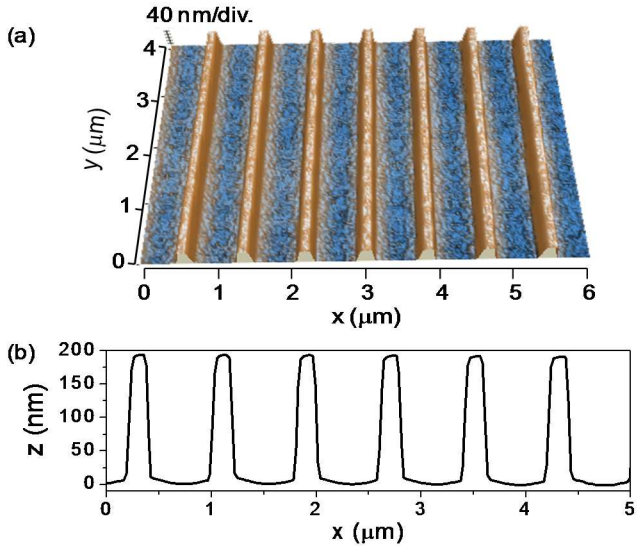

Figure 4-12 (a) AFM image and (b) profile of one of the fabricated Si grating devices; the device parameters are Λ = 798 nm, F = 0.17, and d_g = 193 nm.

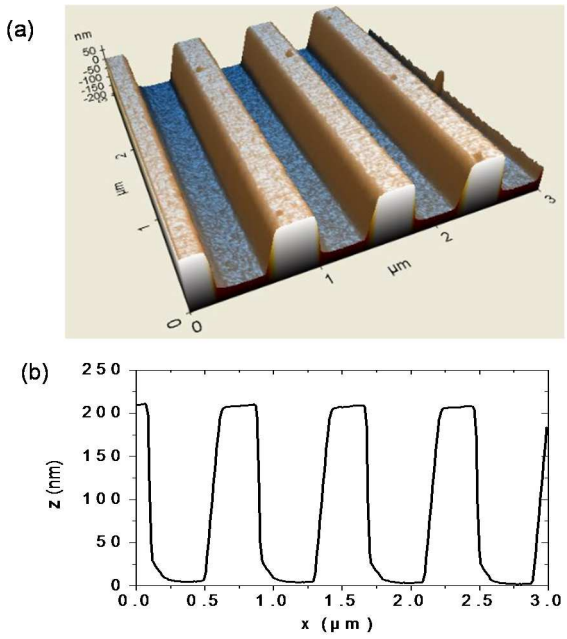

Figure 4-13 (a) AFM image (b) Profile of the fabricated TiO_2 grating; the device parameters are Λ = 800 nm, F = 0.36, and d_g = 209 nm.

(a)

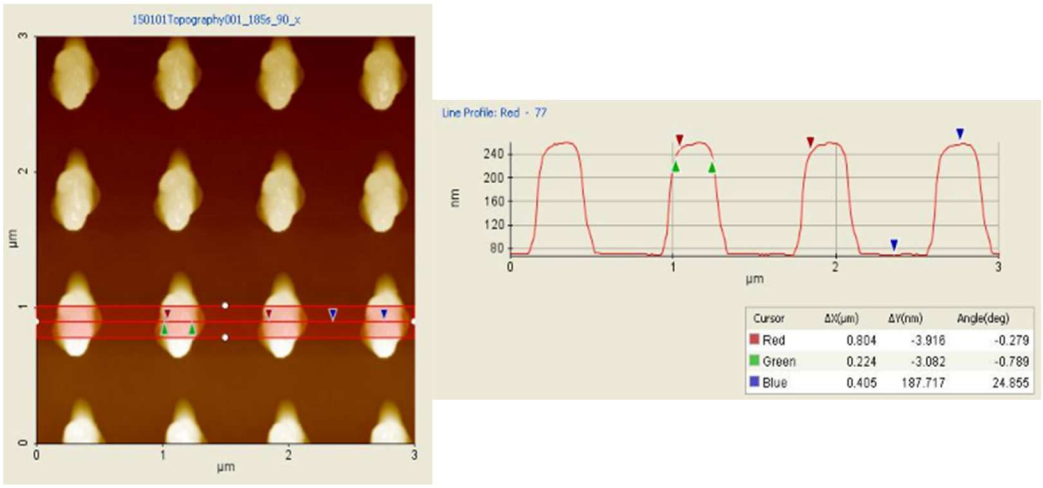

(b)

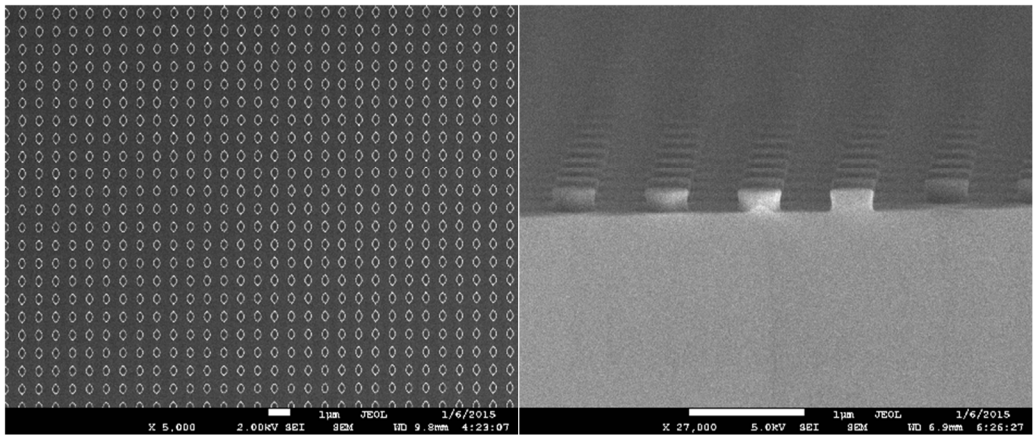

Figure 4-14 (a) AFM image and (b) SEM image of the fabricated 2D multiline GMR devices; the sampled device parameters are Λ = 800 nm, $F_x = F_y = 0.3$, d_g = 190 nm.

4.4 Experimental Results

In the experiments we demonstrate typical results for the design in Section 2.1 and focus our attention on TE polarization. For 1D devices we measure the transmittance

and reflectance of the fabricated sample under TE-polarized light incidence and compare to theoretical prediction. In the optical measurement, we use a supercontinuum Koheras SuperK Compact light source, which covers the 500-2400 nm wavelength range and for collecting spectral data we use an optical spectrum analyzer (Yokogawa AQ6375) operating at a resolution of 0.05 nm.

Figure 4-15 and 4-16 show the simulated and measured spectra for Si and TiO_2 grating devices, respectively. Both devices employ thick Si waveguide and operate across wide spectral bands; we focus on the 1545-1555 nm wavelength range in our investigation. For the Si grating devices, the experimental parameters are approximately Λ = 798 nm, F = 0.3, d_g = 193 nm, n_{AR} = 1.93 and d_{AR} = 203 nm; For the TiO_2 grating devices, the experimental parameters are approximately Λ = 800 nm, F = 0.36, d_g = 209 nm, n_{AR} = 1.9 and d_{AR} = 205 nm. The figures show that experimental spectra for both device types demonstrate good agreement with the simulated spectra in the resonance locations and spectral shape. Reasonable peak efficiency and sideband are achieved for both devices. The TiO_2 devices with lower grating modulation strength $\Delta\varepsilon=n_g^2-n_c^2$ exhibit smaller spectral linewidths as expected. Also, flatter sideband is achieved for TiO_2 grating devices.

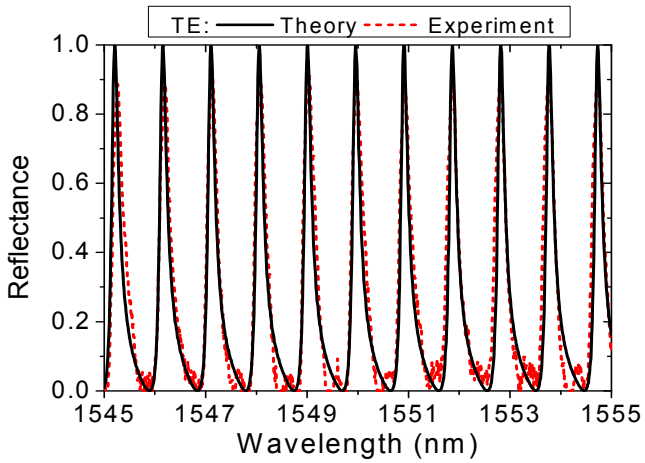

Figure 4-15 Measured vs. simulated reflectance spectra of GMR devices with Si waveguide and Si gratings. Measured parameters are Λ = 798 nm, F = 0.3, d_g = 193 nm, n_{AR} = 1.93, and d_{AR} = 203 nm with corresponding design parameters as Λ = 800 nm, F = 0.16, d_g = 190 nm, n_{AR} = 1.865, and d_{AR} = 208 nm.

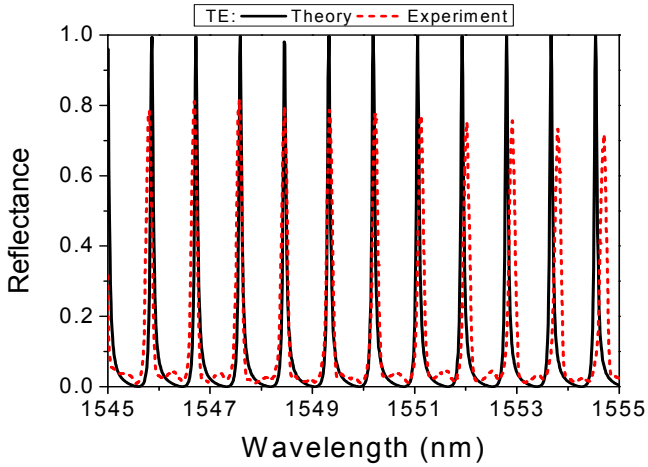

Figure 4-16 Measured vs. simulated reflectance spectra of GMR devices with Si waveguide and TiO_2 gratings. Measured parameters are Λ = 800 nm, F = 0.36, d_g = 209 nm, n_{AR} = 1.9, and d_{AR} = 205 nm. The design parameters are Λ = 800 nm, F = 0.32, d_g = 204 nm, n_{AR} = 1.865, and d_{AR} = 208 nm.

Figure 4-17 shows the preliminary results we obtained for 2D multiline GMR devices. We sample the 1545-1555 nm wavelength range in our investigation. The experimental parameters are Λ = 800 nm, $F_x = F_y = 0.3$, d_g = 190 nm. The figures show that at both TE and TM polarization we can obtain similar multiline spectra that preliminarily demonstrate the polarization-independence characteristics. The spectra don't show sharp TM peaks due to the resolution of the test tools.

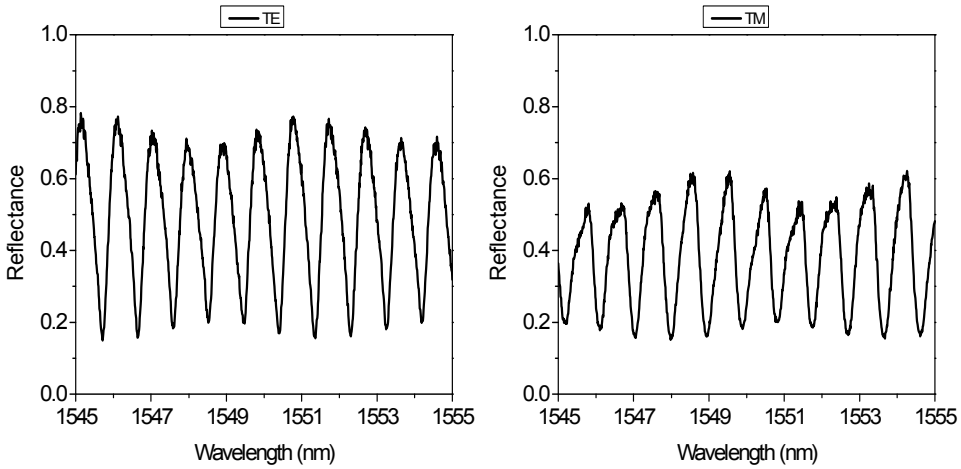

Figure 4-17 Measured reflectance spectra of 2D multiline GMR devices on unpolarized light incidence. Measured parameters are Λ = 800 nm, $F_x = F_y = 0.3$, d_g = 190 nm.

We also preformed multiple experiments on cascaded multiline devices and angular shift. We measured both the individual filter as well as the cascaded devices spectra, as shown in Figure 4-18. On each sample Au is deposited beside the device area to act as a nearly perfect mirror. By setting up one of the two devices as a mirror, we can obtain a spectrum for one single device. We measure reflectance of the fabricated samples under TE-polarized light incidence. In the measurement, we use a supercontinuum Koheras SuperK Compact light source, which covers the ~500- to 2400-

nm wavelength range and an optical spectrum analyzer (Yokogawa AQ6375) operating at a resolution of 0.05 nm.

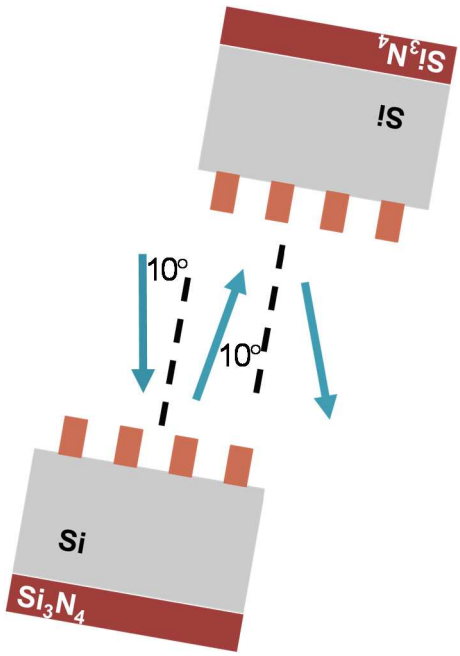

Figure 4-18 Schematic illustration of spectral measurement of cascaded multiline devices.

Figure 4-19 shows calculated and measured spectral response after one single device. From the dashed curve for the experimental spectrum we can observe that a peak efficiency of ~ 0.9 and an FWHM linewidth of ~0.2 nm are obtained. The sideband rejection is between – 15 and – 20 dB over the measurement range of 10nm. The numerical result of solid curve is obtained by rigorous coupled-wave analysis (RCWA) approximately using Λ = 800 nm, F = 0.16, d_g = 190 nm, n_{AR} = 1.865, and d_{AR} = 208 nm. The figure denotes that the measured spectra show reasonable agreement with the simulated spectra, particularly for the resonance wavelength locations and bandwidths of individual spectral peaks.

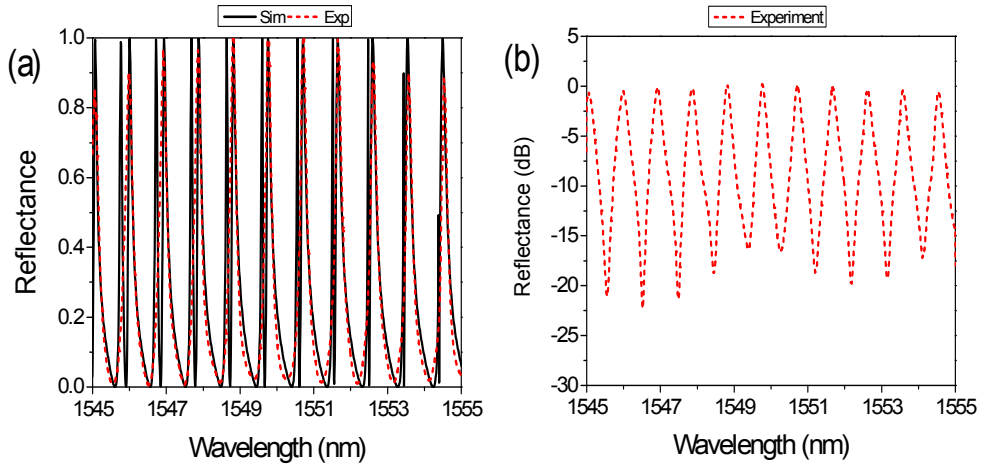

Figure 4-19 Measured and simulated individual GMR device (a) reflectance and (b) reflectance in dB spectra. Measured parameters are Λ = 798 nm, F = 0.17, d_g = 193 nm, n_{AR} = 1.93, and $_{dAR}$ = 203 nm. Fitting parameters are Λ = 800 nm, F = 0.16, d_g = 190 nm, n_{AR} = 1.865, and d_{AR} = 208 nm. Incidence angle θ = 10° .

Figure 4-20 shows calculated and measured spectral response after two cascaded devices. From the experimental spectra we can observe that a peak efficiency of ~ 0.8 and an FWHM linewidth of ~0.15 nm are obtained. The sideband rejection is between – 25 and – 30 dB over the measurement range of 10nm. The cascaded devices parameters are Λ = 798 nm, F = 0.17, d_g = 193 nm and Λ = 800 nm, F = 0.2, d_g = 195 nm, respectively. As compared with individual device the linewidth is reduced by ~ 25% and the sideband lowered by ~ -10 dB at the expense of peak efficiency dropping by ~ 0.1.

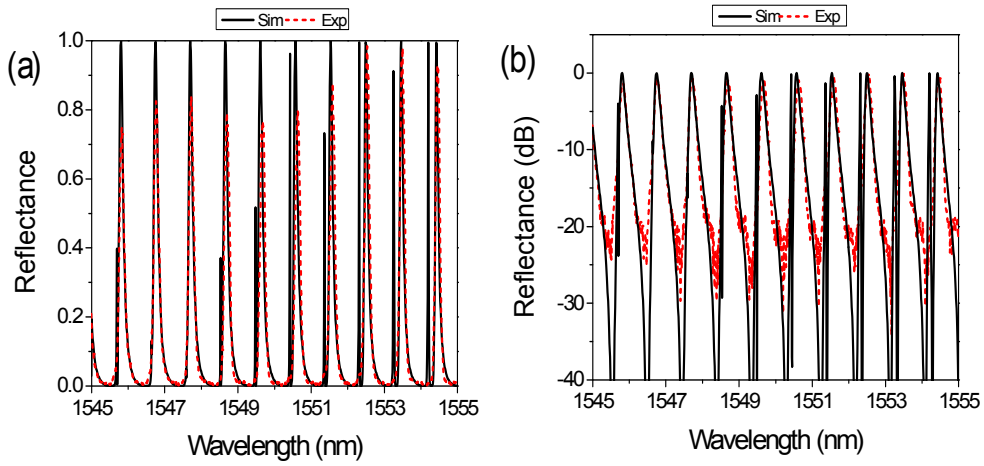

Figure 4-20 Measured and simulated cascaded GMR device (a) reflectance and (b) reflectance in dB spectra. Measured parameters are Λ = 798 nm, F = 0.17, d_g = 193 nm and Λ = 800 nm, F = 0.2, d_g = 195 nm, respectively. Fitting parameters are Λ = 800 nm, F = 0.16, d_g = 190 nm, n_{AR} = 1.865, and d_{AR} = 208 nm. Incidence angle $\theta_1 = \theta_2 = 10°$.

For the angular shift investigation, we select the 1545-nm to 1555-nm wavelength range for the input wave spectrum and small incidence angle is assumed. For small angle incidence (< 20°) AR layer works well and the spectra are not affected significantly by the angle except from the peak splitting effect. For this investigation we ignore the peak splitting phenomenon and focus on the angularly peak shifting. We compute the peak shift using RCWA. Figure 4-21 shows the simulation result of peak shifting within considered wavelength range. From the figure we can clearly see that the resonance peak is shifting one whole free spectral range (FSR) under the variation of incidence angle from 9.92° to 10.15°. Due to the periodic characteristics of resonance peaks the angular shift can cover a very broad wavelength range of several hundred nanometers.

We measure the angular reflectance of the fabricated sample under TE-polarized light incidence. Incidence angles are the same as in the simulation i.e. θ = 9.92°, 10.04°, 10.15°. In the optical measurement, we use a supercontinuum Koheras SuperK Compact light source, which covers the ~500-nm to 2400-nm wavelength range and an optical spectrum analyzer (Yokogawa AQ6375) operating at a resolution of 0.05 nm. Figure 4-22 shows the measured angular reflectance spectrum. The experimental spectra fit the numerical results approximately using Λ = 800 nm, F = 0.17, d_g = 190 nm, n_{AR} = 1.9, and d_{AR} = 190 nm. The figures denote that the measured spectra show reasonable agreement with the simulated spectra, from 9.92° to 10.15° the resonance peak move from ~ 1551nm to ~ 1552nm, i. e. one FSR as shown in Figure 4-21.

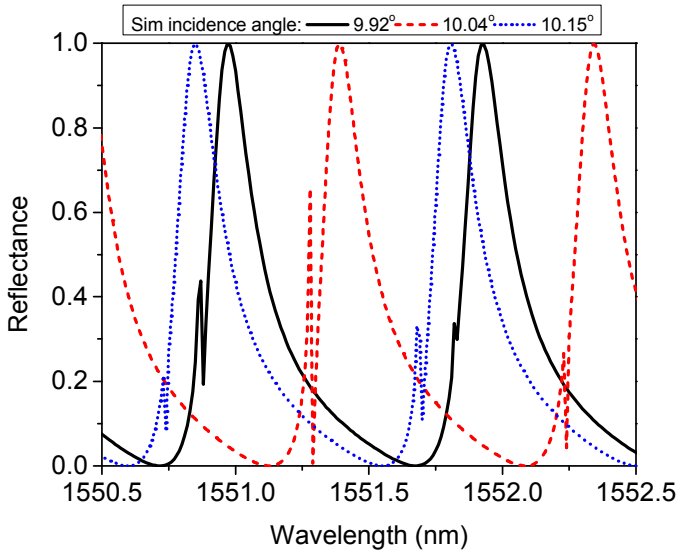

Figure 4-21 Calculated peak shiftting spectrum of multiline GMR device. Transverse-electric (TE) polarization, with the electric vector normal to the plane of incidence, is assumed for the incident light. Device parameters of the GMR filter are Λ = 0.8 μm, F = 0.2, d_g = 0.19 μm, d = 300 μm, n = 3.48, n_{AR} = 1.865, and d_{AR} = 0.208 μm.

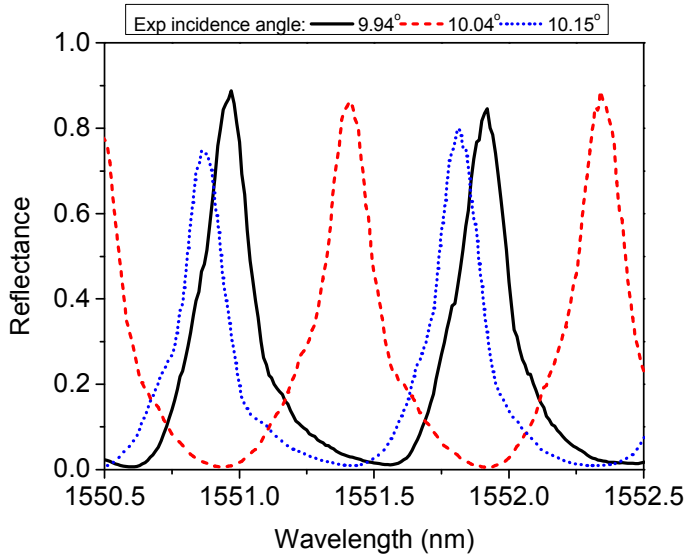

Figure 4-22 Measured peak shifting spectrum of multiline GMR device. Transverse-electric (TE) polarization, with the electric vector normal to the plane of incidence, is assumed for the incident light. Device parameters of the GMR filter are Λ = 0.8 μm, F = 0.17, d_g = 190 nm, n_{AR} = 1.9, and d_{AR} = 190 nm.

Figure 4-23 and figure 4-24 shows the simulation and experimental results of thermally tunable characteristics of GMR multiline devices. By heating up the devices we can move the resonance peaks. As seen from the figures heating up the device by ~50K we can move the resonance peak by ~0.5nm.

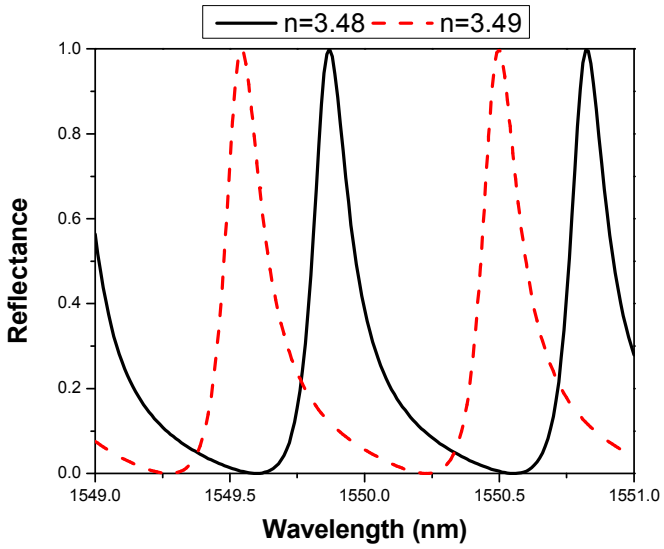

Figure 4-23 Simulated resonance peak shift by heating up the device.

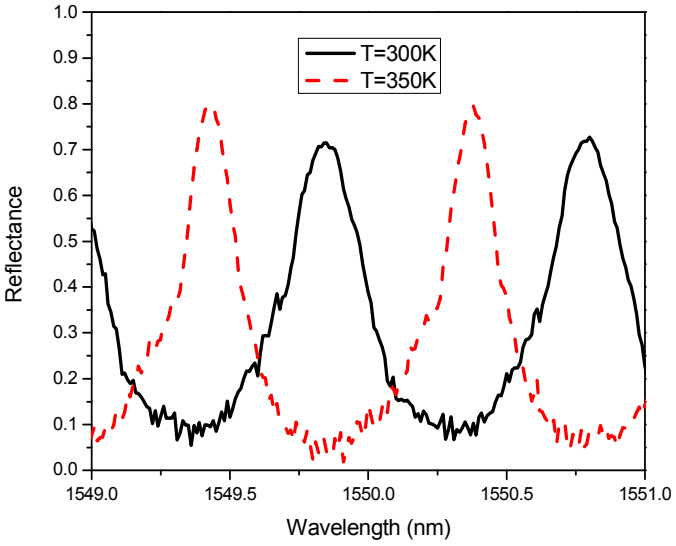

Figure 4-24 Measured resonance peak shift by heating up the device.

4.5 Applications

There are many applications for GMR multiline devices such as laser mirrors, which were demonstrated in Chapter 3, signal processor which will be shown in the next chapter, and gas sensor which is presented here in more detail. The application as gas sensors by GMR multiline devices can be accomplished by matching the absorption spectrum of the gas of interest to a proper GMR multiline filter. One reason that the multiline filter is needed for gas sensors is that directly using broad light source covers interfering gases leading to cross gas issue. The other, is that directly using broad light source makes the power variation caused by gas absorption too small to be detected. So we need to filter the broad light spectrum to match the absorption lines of the specified gas. A design example of gas sensor for CH_4 is shown as following. Figure 4-25 shows the CH_4 absorption spectrum within a specified wavelength range of 1.63μm ~ 1.67μm. Figure 4-26 and figure 4-27 show the design example of GMR multiline spectrum to match the gas absorption spectrum.

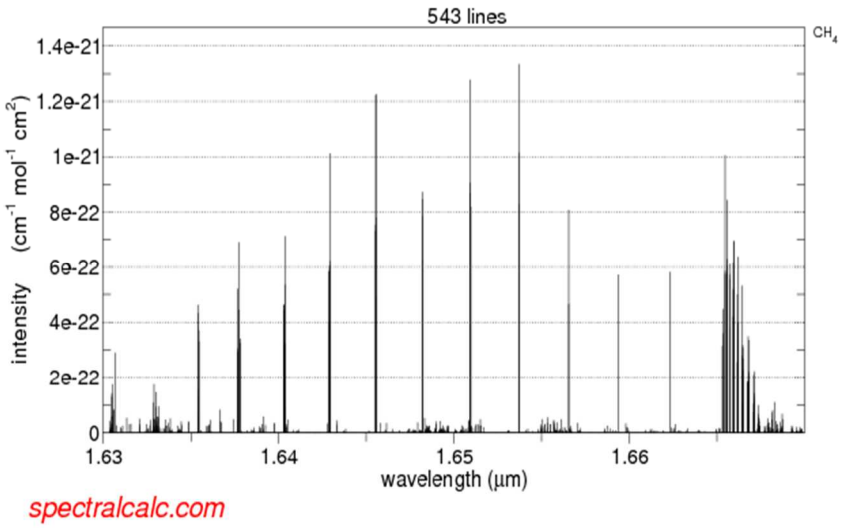

Figure 4-25 CH_4 absorption spectrum within a specified wavelength range of 1.63μm ~ 1.67μm. [Data from: http://spectralcalc.com/spectral_browser/db_intensity.php]

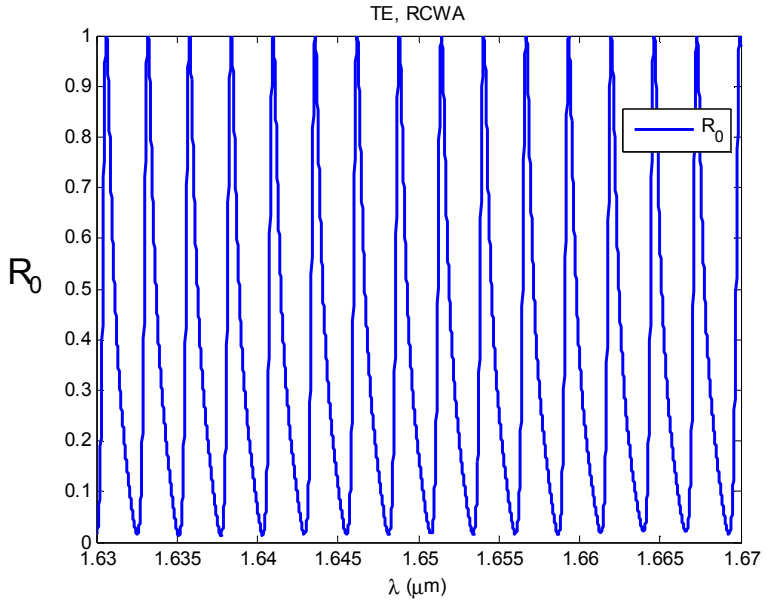

Figure 4-26 Designed GMR multiline spectrum.

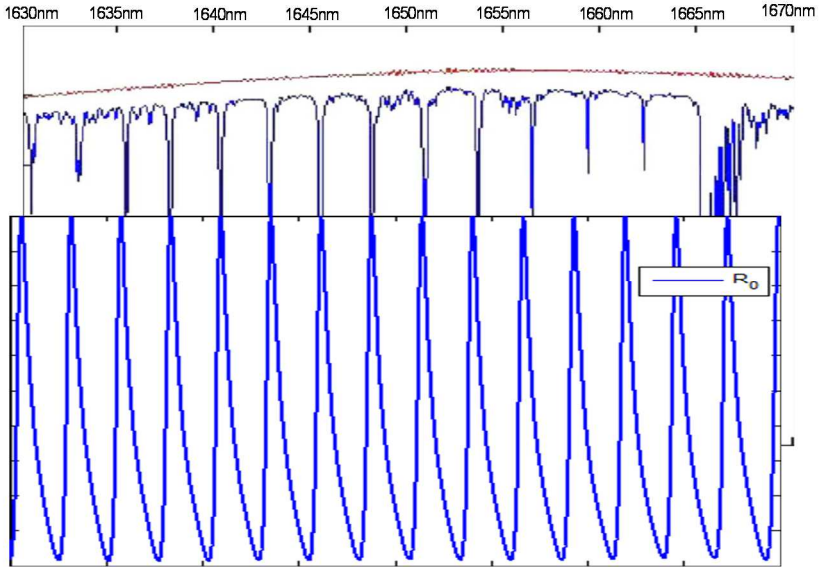

Figure 4-27 GMR multiline spectrum matched to the CH_4 absorption spectrum.

4.6 Conclusion

In conclusion, simulated and experimental spectral properties of multiline guided-mode resonators are presented based on various applications. There is a reasonable match between theory and experiment. Possible applications include spectral sampling and wavelength discretization. In sensing gas species and evaluating attendant concentrations, cross gas mitigation may be needed to ascertain detection and quantification of the species of interest while excluding others. This can be accomplished by matching the absorption spectrum of the gas of interest to a proper multiline filter [60]. Important in mine safety and some industrial control processes, optical monitoring of methane gas concentrations has recently been accomplished using matched comb filtering. In one case this was implemented by a Sagnac loop filter [60], and in the other by a high-finesse Fabry-Perot filter [61]. In optical communication systems RZ to NRZ signal conversion is the key technology for the requirement of connecting between optical time-division multiplexing network employing RZ format and wavelength-division multiplexing network employing NRZ format. This can be implemented by employing different multiline filters, in one example by MKR(micro knot resonator)[62] and in the other by ring resonator[63]. GMR multiline filters have analogous application potential in above systems as spectral range, resonance peak locations, bandwidth, and sideband levels are readily matched to the specific spectral lines by tuning key geometrical parameters.

Cascaded Si-based multiline GMRF devices are calculated and measured. Reasonable match between simulation and experiments are achieved. From the experiments compared with individual devices the cascaded devices linewidth FWHM is reduced by ~ 25% and the sideband lowed by ~ -10 dB at the expense of peak efficiency dropping by ~ 0.1. The improvement in sideband level rejection and linewidth FWHM can

make this new type of multiline GMRF devices possess great potential for optical communication and high sensitivity gas sensor system.

Angular tunability of Si-based multiline GMRF devices are also calculated and measured. Reasonable match between simulation and experiments are achieved. From the experiments we can conclude that within a small variation of incidence angle the resonance peak can shift for one whole FSR. The tunability can make this new type of multiline GMRF devices possess great potential for mode-competing multiline laser and high sensitivity gas sensor system. Combined with application in [59] the laser lines can be tuned not only on different resonance peaks but also between the peaks, thus a very broad tuning wavelength range can be covered that is determined by periodic multiple peaks. In another aspect, for gas sensing and signal processing application the specific spectral lines of interest is matched to a proper comb filter [60,61,62,63]. In GMR devices the tunability of the multiple resonance peaks can relax the difficulty of matching the sharp resonance peaks to the specific spectral lines.

In future research, fabrication of polarization independent 2D devices and Brewster devices are contemplated.

Chapter 5

RZ to NRZ Signal Conversion Utilizing Guided-mode Resonance Devices

5.1 Introduction

Resonance effects constitute the fundamental phenomena in optics and photonics. Originated from traditional diffractive optics, the guided-mode resonance (GMR) effect has been investigated for several decades [64,65,66]. Various models and numerical methods have been developed to analyze and understand pertinent device embodiments [67,68]. Based on numerical models, resonant structures have been designed with applications including energy [69], information technology [70], and resonant sensors [71]. In future optical communication system[s] all-optical networks may be required to support a variety of modulation and data formats. Two standard data formats that are fairly mature and widespread in current optical transmission systems are the return-to-zero (RZ) and non-return-to-zero (NRZ) formats. Various all-optical conversion schemes from RZ to NRZ have been demonstrated to provide an important interface technology at the nodes of wavelength division multiplexing (WDM) and optical time division multiplexing (OTDM) networks [72,73,74]. In this chapter, we apply multiline GMR devices that support multiple simultaneous resonances to implement the conversion. Also GMR reflection and transmission filters with single resonance peaks are investigated to implement the conversion. Due to GMR devices' simple, compact characteristics they can be a good alternative for the conversion both in free space and on chip.

A recent study furnished a quantitative evaluation of the resonance properties of very thick resonance elements [14]. Accordingly, here we employ a thick Si waveguide grating that can support thousands of modes in the near-infrared spectral domain. The resulting filter possesses a dense population of resonant states with relatively narrow

resonance bandwidths of individual spectral lines. We design a resonant device using rigorous coupled-wave analysis (RCWA) and apply it to implement RZ to NRZ signal conversion. We achieve preliminary results by using MATLAB simulations. Furthermore we prove that using one common Gaussian filter can also implement RZtoNRZ conversion but the converted signal shows much larger oscillation. To further improve the signal conversion performance, we design GMR filter that possesses the optimal spectral shape of FBG filter in [74].

5.2 Design and Simulation

5.2.1 RZtoNRZ Conversion by Two Cascading Filters – GMR Multiline Filter and Gauss Filter

We adopt the GMR device design in Chapter 4.2.1 to implement RZ to NRZ signal conversion. We simulate the complete conversion flow using MATLAB and the spectral data of GMR multiline device is directly input into the MATLAB codes. The following formula and figures show the whole process.

Consider an N random bit sequence RZ data signal, we generate them by employing a sine function to obtain non-ideal square waveform [75]:

$$s_n(RZ) = g_n \sin\{0.5\,\pi\,[\sin(2\,\pi\,f_s\,t + \phi_0)]^2\} \quad (5.1)$$

where g_n = [0, 1], n = 1, 2, … , N; f_s is the bit rate, ϕ_0 is the initial phase, default = 0. g_n = [0, 1], n = 1, 2, … , N; Figure 5-1 (a) shows the time domain signal waveform.

By performing discrete Fourier transform (DFT) [76] to the time signal we can obtain the frequency domain signal magnitude as expressed as:

$$Q_{RZ}(f) = \sum_{n=1}^{N} s_n e^{-i2\pi fn}\ ,\ f \in \{1/N, 2/N, \dots 1,\} \quad (5.2)$$

Thereafter we calculate the power spectrum of frequency domain signal by:

$$P = Q_{RZ}\ \mathrm{conj}(Q_{RZ}) / T \quad (5.3)$$

where T is the time period. The power spectrum of RZ signal is shown in Figure 5-1(b).

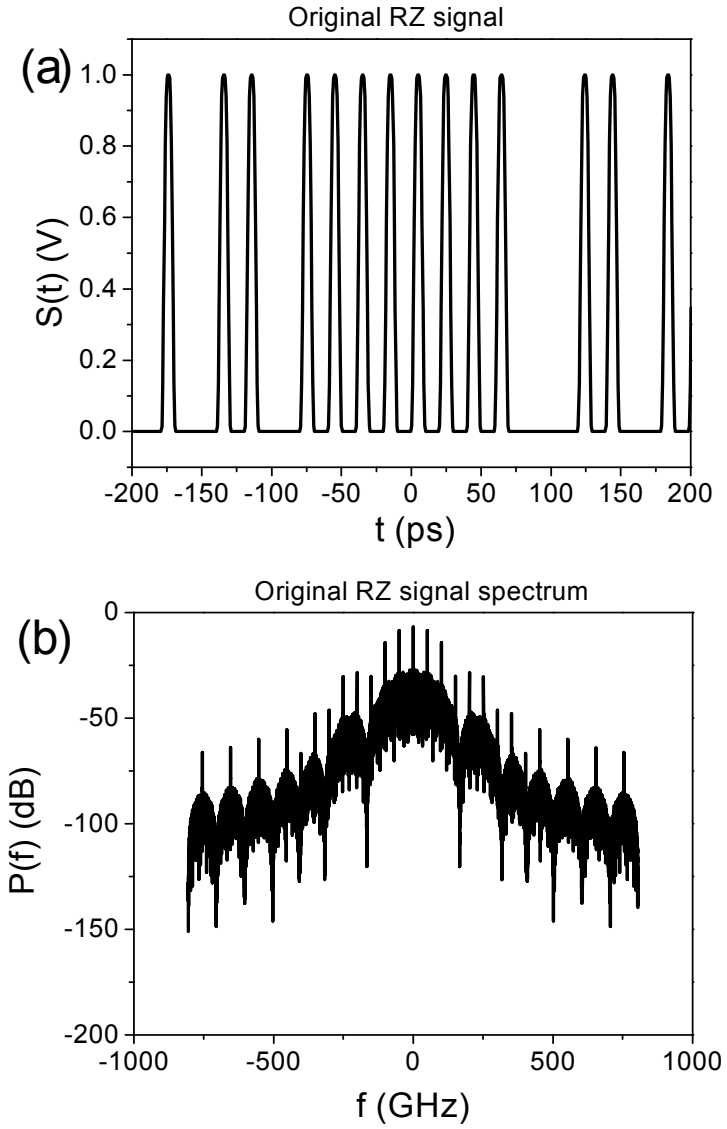

Figure 5-1 RZ signal time (a) and frequency (b) domain waveform.

In the conversion flow as shown in Figure 5-2 we employ 2 cascaded filters, the multiline filter and the Gaussian filter. Figure 5-2(a) shows the multiline filter spectrum and the RZ signal spectrum from which we can see the spectral lines of multiline filter match well with the sideband spikes of the RZ signal spectrum. Thus the sideband peaks of RZ signal can be removed. Figure 5-2(b) shows the RZ signal spectrum after the

multiline filter and the Gaussian filter spectrum that is adopted to do the second filtering, namely narrowing the sideband further. From Figure 5-2(c) we can see that after two filters the RZ signal spectrum's sideband spikes are all removed and the whole spectrum is becoming much narrower. In the conversion we input the multiline filter's spectral data from the simulation result by RM_solver software and the Gaussian filter is generated by normal distribution as described in (5.5).

$$P\_MLF = 10 \log_{10}(P) + 10 \log_{10}(MLF\_data) \quad (5.4)$$

where P_MLF is the power spectrum in dB after multiline filter. MLF_data is input from RM_solver simulation.

$$P\_Gauss = P\_MLF + 10 \log_{10}\left[\exp(-x^2 / 2\sigma^2) / (\sigma \sqrt{2\pi}) \right] \quad (5.5)$$

where P_Gauss is the power spectrum in dB after Gaussian filter. σ=0.02 is the standard deviation.

After filtering RZ signal spectrum is converted to spectrum as shown in Figure 5-2(c). We perform Inverse Discrete Fourier Transform (IDFT) to achieve NRZ signal time domain waveform as described in

$$s_n(NRZ) = \frac{1}{N} \sum_{k=1}^{N} Q_{NRZ}\left(\frac{k}{N}\right) e^{-i2\pi \frac{k}{N} n} \text{ , } n \in \{1, 2, \ldots N,\} \quad (5.6)$$

where $Q_{NRZ}(f) = \sqrt{T\ 10^{\frac{P\_Gauss}{10}}}\ \exp(i\,\theta)$ is the NRZ signal magnitude, $\Theta = \text{angle}(Q_{RZ}(f))$ is the phase angle of $Q_{RZ}(f)$. The obtained NRZ time domain signal is shown in Figure 5-3.

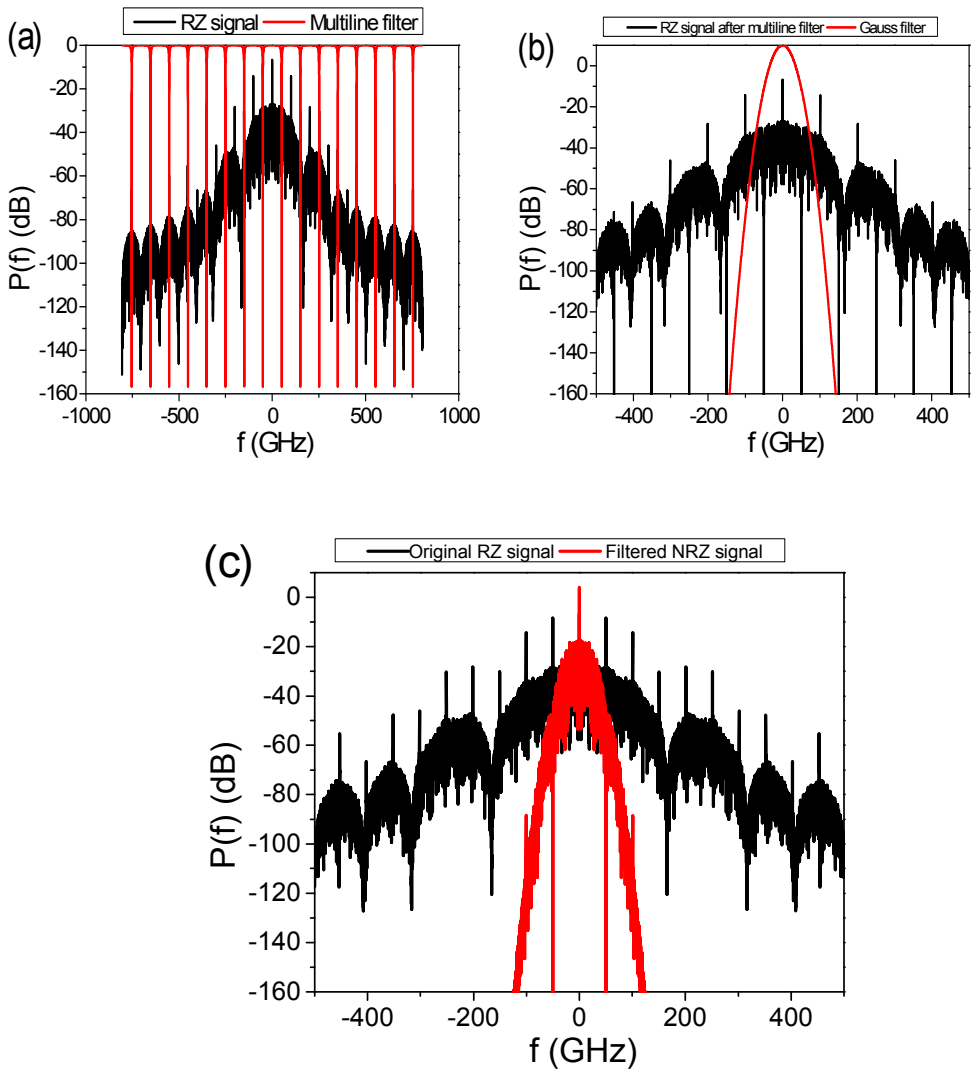

Figure 5-2 RZ to NRZ spectrum conversion flow by employing multiline and Gaussian filters. (a) Original RZ signal and matching multiline filter. (b) Spectrum after multiline filtering and employed Gaussian filter. (c) RZ signal and converted NRZ signal spectra.

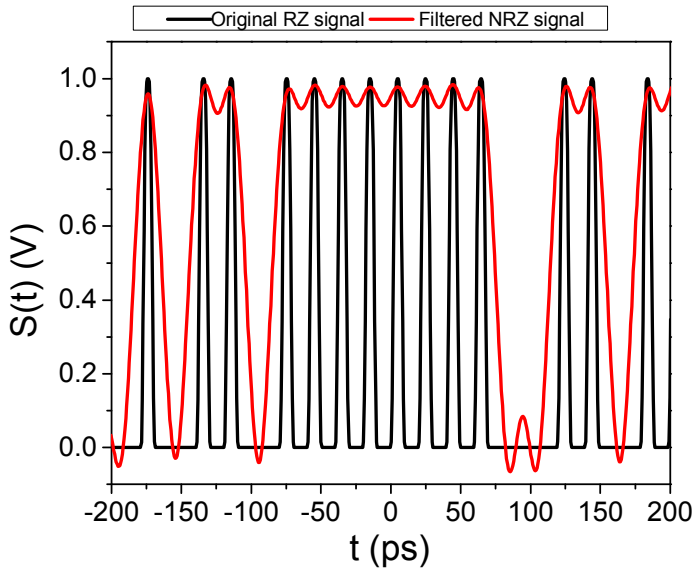

Figure 5-3 Original RZ signal and converted NRZ signal time domain waveforms.

5.2.2 RZtoNRZ Conversion by Single Filter

In [74] using only one filter to implement RZtoNRZ conversion was demonstrated. An optimally designed fiber Bragg grating (FBG) filter was employed to make the conversion. In this work, by simulation, we prove that an individual filter possessing Gaussian shape can also realize the conversion. Furthermore, we design GMR filters to possess spectral shape matched to the FBG filter spectrum. By doing this we can prove that one individual GMR filter (reflection or transmission) can implement RZtoNRZ conversion with good performance.

Figure 5-4 shows the RZtoNRZ conversion simulation results using an individual common Gaussian filter. It is clear that this single Gaussian filter does realize the RZtoNRZ conversion, but the resultant signal shows much larger oscillation compared to the results obtained by using both multiline and Gauss filter. The latter is due to the removal of sideband spikes by the multiline filter.

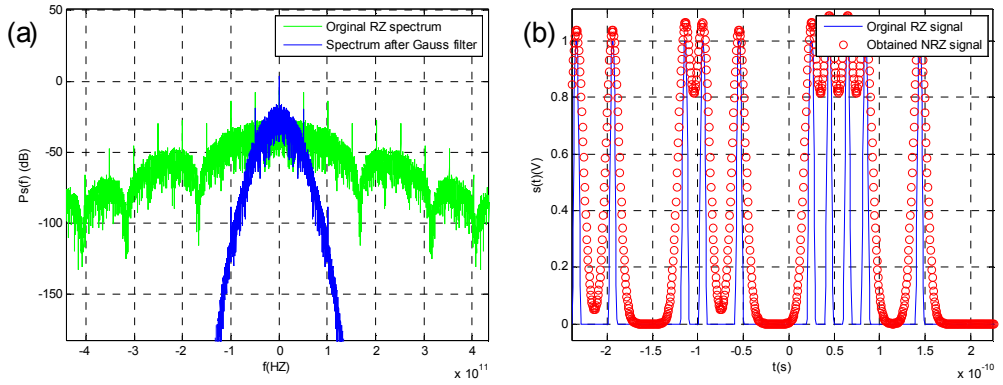

Figure 5-4 RZ to NRZ signal conversion by one common Gaussian filter. (a) Spectra for RZ and NRZ signals. (b) Time domain waveforms for RZ and NRZ signals.

To further improve the signal conversion performance, we designed a GMR filter that possesses the optimal spectral shape of FBG filter as shown in Figure 5-5 [74]. We designed two different types of filters to match the spectrum, one is the GMR reflection filter and the other is the GMR transmission filter. Figure 5-6 shows the designed GMR reflection filter structure and its corresponding spectrum. Figure 5-7 shows the matching of the designed GMR reflection filter and optimal target filter spectrum. Figure 5-8 shows the designed GMR transmission filter structure and its corresponding spectrum. Figure 5-9 shows the matching of the designed GMR transmission filter and optimal target filter spectrum.

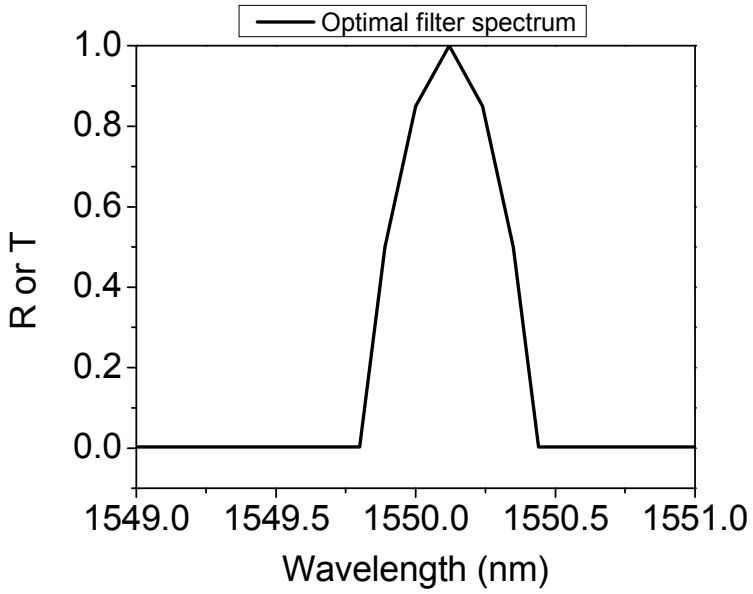

Figure 5-5 optimally designed FBG filter spectrum.

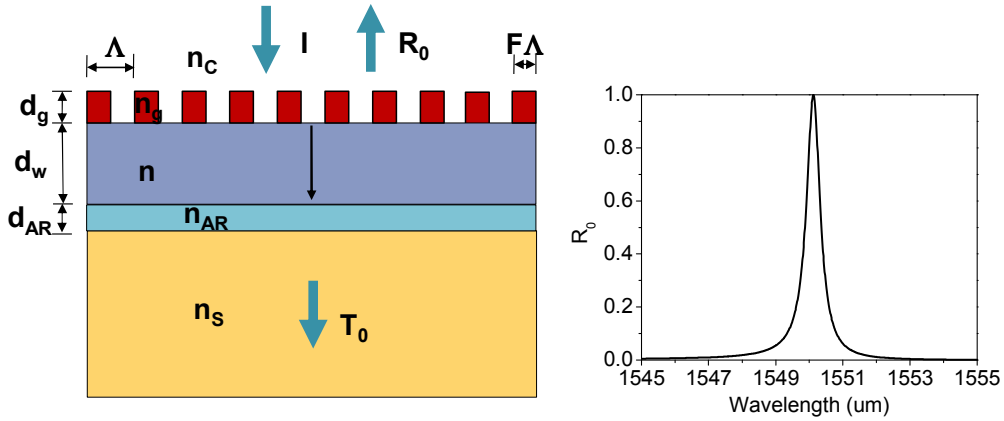

Figure 5-6 Designed GMR reflection filter structure and its corresponding spectrum. The design parameters are Λ = 998.1 nm, F = 0.4, d_g = 200 nm, n_g = 2.5, d_w = 300 nm, n = 3.5, n_{AR} = 2.2, and d_{AR} = 166 nm, n_{sub} = 1.5.

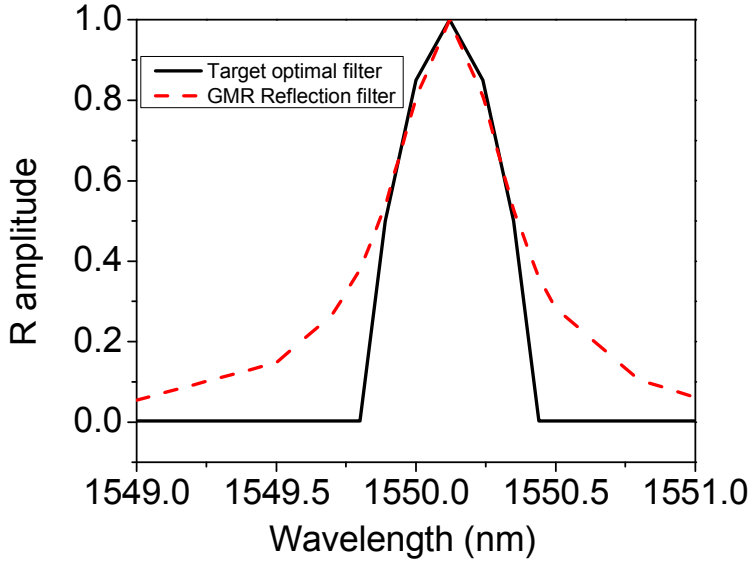

Figure 5-7 Designed GMR reflection filter and target optimal filter spectrum.

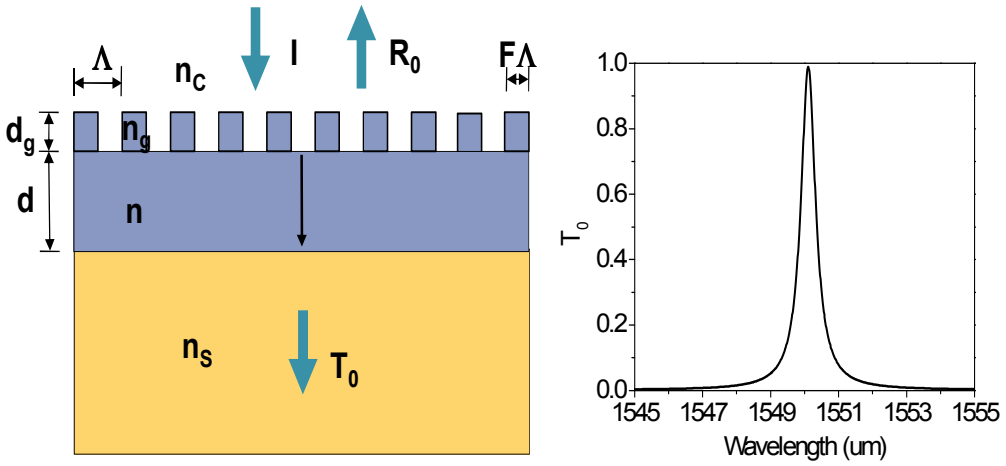

Figure 5-8 Designed GMR transmission filter structure and its corresponding spectrum.

The design parameters are Λ = 1015 nm, F = 0.25, d_g = 330 nm, n_g = 3.5, d_w = 290 nm, n = 3.5, n_{sub} = 1.5.

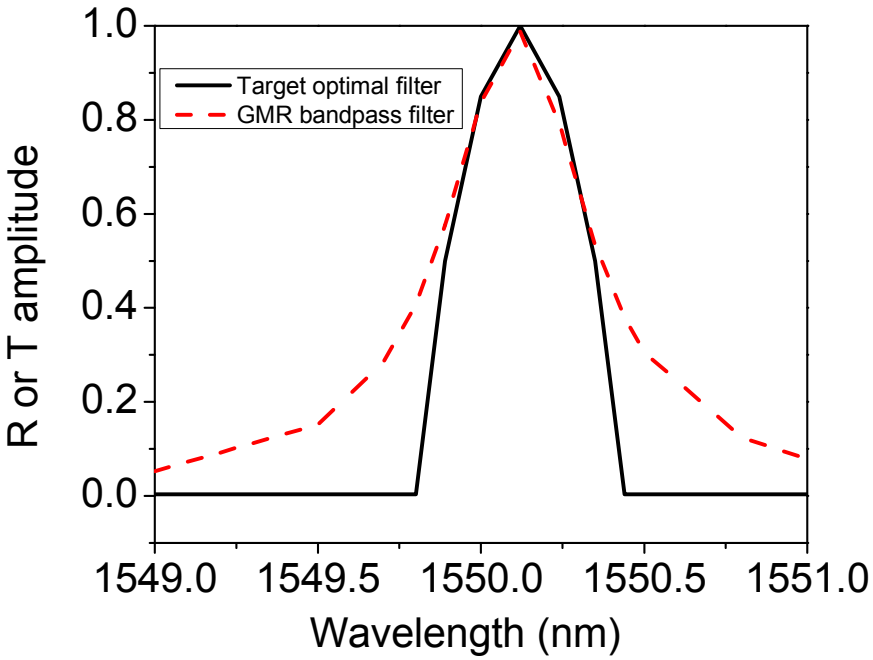

Figure 5-9 Designed GMR bandpass filter and target optimal filter spectrum.

Chapter 6

Conclusions and Future Directions

In this dissertation, new GMR devices and applications are investigated.

Prototype thermoelectric devices incorporating resonant absorbers are presented. They are compared to unpatterned and random-surface devices to verify performance enhancement. Simulation results show that the integrated resonant segments enhance the performance appreciably compared to the reference devices for both device classes tested. Additional research is needed to develop this concept further and optimize the design and fabrication for improved electrical output. These resonance-enhanced thermoelectric elements are simple and compact and may be useful in thermopile systems and as voltage generators or IR sensors.

A wavelength-selective external cavity laser using a multiline GMR filter as the laser mirror is presented. The experimental results demonstrate that a stable selective laser line can be generated from every resonance peak of the GMR multiline device. As reasonable agreement is found between the multiline device's generated laser lines and their corresponding resonance peaks, these preliminary results verify the applicability of multiline GMR devices. Investigation of analogous resonance structures using other material systems and spectral regions may extend the application potential of this device class.

In much details simulated and experimental spectral properties of multiline guided-mode resonators are presented based on various applications. There is reasonable match between theory and experiment. Possible applications include gas sensors and signal processors as spectral range, resonance peak locations, bandwidth, and sideband levels are readily matched to the specific spectral lines by tuning key geometrical parameters. Cascaded Si-based multiline GMRF devices are calculated and

measured. Reasonable match between simulation and experiments are achieved. Angular tunability of Si-based multiline GMRF devices are also calculated and measured. Reasonable match between simulation and experiments are achieved. In future research, fabrication of polarization independent 2D devices and Brewster devices are contemplated.

Implementation of RZ to NRZ signal conversion in optical communication by employing GMR devices is discussed in theory. We realize the conversion by two solutions. By the first solution, RZtoNRZ conversion is done by two cascading filters – GMR multiline filter and Gauss filter. By the second solution, we prove that an individual filter possessing Gaussian shape can also realize the conversion. Furthermore we design GMR filters to possess spectral shape matched to the referred optimal FBG filter spectrum to obtain better performances. Further research may be considered on improving GMR filter performances and experimental verification.

References

[1] E. Hecht, Optics, 4th ed, Addison Wesley, San Francisco, 2002.

[2] P. Vincent and M. Neviere, “Corrugated dielectric waveguides: A numerical study of the second-order stop bands,” Appl. Phys. vol. 20, pp. 345-351, 1979.

[3] L. Mashev and E. Popov, “Zero order anomaly of dielectric coated gratings,” Opt. Comm. vol. 55, pp. 377-380, 1985.

[4] A. Avrutsky and V. A. Sychugov, “Reflection of a beam of finite size from a corrugated waveguide,” J. Mod. Opt. vol. 36, pp. 1527-1539, 1989.

[5] S. S. Wang and R. Magnusson, “Theory and applications of guided-mode resonance filters,” Appl. Opt. vol. 32, pp. 2606-2613, 1993.

[6] T. Khaleque, H. Svavarsson, and R. Magnusson, “Fabrication of resonant patterns using thermal nano-imprint lithography for thin-film photovoltaic applications,” Optics Express—Energy, vol. 21, pp. A631-A641, 2013.

[7] D. Shin, S. Tibuleac, T. A. Maldonado, R. Magnusson, “Thin film optical filters with diffractive elements and waveguides,” Opt. Eng. vol. 37, pp. 2634-2646, 1998.

[8] D. Wawro, S. Tibuleac, R. Magnusson, and H. Liu, “Optical fiber endface biosensor based on resonances in dielectric waveguide gratings,” in Proc. SPIE, Biomedical Diagnostic, Guidance, and Surgical-Assist Systems II, San Jose, Calif., vol. 3911, pp. 86-94, May 2000.

[9] T. K. Gaylord and M. G. Moharam, “Analysis and application of Optical Diffraction by Gratings,” Proc. IEEE, vol. 73, pp. 894-937, 1985.

[10] D. Rosenblatt, A. Sharon, and A. A. Friesem, “Resonant grating waveguide structures,” IEEE J. Quan. Elec. vol. 33, pp. 2038-2059, 1997.

[11] D. Kraemer, B. Poudel, H. P. Feng, etc “High performance flat panel solar thermoelectric generators with high thermal concentration,” Nature Materials, vol. 10, pp. 532-538, 2011.

[12] S. Ogawa, K. Okada, N. Fukushima, and M. Kimata, “Wavelength selective uncooled infrared sensor by plasmonics,” Applied Physics Letters, vol. 100, pp. 021111, 1-4, 2012.

[13] B. E. A. Saleh, M. C. Teich, Fundamentals of Photonics: 2nd Ed. (John Wiley & Sons), 2007.

[14] R. Magnusson, “Spectrally dense comb-like filters fashioned with thick guided-mode resonant gratings,” Opt. Lett., vol. 37, no. 18, pp. 3792-3794, Sept. 2012.

[15] A. Kosuga, K. Nakai, M. Matsuzawa, Y. Fujii, R. Funahashi, T. Tachizawa, Y. Kubota, and K. Kifune, “Enhanced thermoelectric performance of In-substituted GeSb6Te10 with homologous Structure,” APL Mater., vol. 2, no. 8, pp. 086102-1–086102-7, Aug. 2014.

[16] G. Pennelli, “Review of nanostructured devices for thermoelectric applications,” Beilstein J. Nanotechnol., vol. 5, pp. 1268–1284, Aug. 2014.

[17] S. Wang, Solid-state Electronics, McGraw-Hill Inc., New York, 1966.

[18] D. Kraemer, B. Poudel, H. P. Feng, J. C. Caylor, B. Yu, X. Yan, Y. Ma, X. Wang, D. Wang, A. Muto, K. McEnaney, M. Chiesa, Z. Ren, and G. Chen, “High performance flat panel solar thermoelectric generators with high thermal concentration,” Nature Materials, vol. 10, pp. 532-538, May. 2011.

[19] S. Ogawa, K. Okada, N. Fukushima, and M. Kimata, “Wavelength selective uncooled infrared sensor by plasmonics,” Appl. Phys. Lett., vol. 100, no. 2, pp. 021111-1─021111-4, Jan. 2012.

[20] D. Xu, B. Xiong, and Y. Wang, “Micromachined thermopile IR detector Module with High Performance,” IEEE Photon. Technol. Lett., vol. 23, no. 3, pp. 149-151, Feb. 2011.

[21] M. Mizoshiri, M. Mikami, K. Ozaki, and K. Kobayashi,“Thin-Film Thermoelectric Modules for Power Generation Using Focused Solar Light,” Journal of Electron. Mater., vol. 41, no. 6, pp. 1713-1719, Apr. 2012.

[22] L. A. Weinstein, K. McEnaney, and G. Chen, “Modeling of thin-film solar thermoelectric generators,” J. Appl. Phys., vol. 113, no. 16, pp. 164504-1─164504-8, Apr. 2013.

[23] J. Xie, C. Lee, and H. Feng, “Design, fabrication, and characterization of CMOS MEMS- Based thermoelectric power generators,” J. Microelectromech. Syst., vol. 19, no. 2, pp. 317-324, Apr. 2010.

[24] P. Vincent and M. Neviere, “Corrugated dielectric waveguides: A numerical study of the second-order stop bands,” Appl. Phys., vol. 20, no. 4, pp. 345-351, Dec. 1979.

[25] L. Mashev and E. Popov, “Zero order anomaly of dielectric coated gratings,” Opt. Comm., vol. 55, no. 6, pp. 377-380, Oct. 1985.

[26] I. A. Avrutsky and V. A. Sychugov, “Reflection of a beam of finite size from a corrugated waveguide,” J. Mod. Opt., vol. 36, no. 11, pp. 1527-1539, Jan. 1989.

[27] Y. Ding and R. Magnusson, “Resonant leaky-mode spectral-band engineering and device applications,” Opt. Express., vol. 12, no. 23, pp. 5661-5674, Nov. 2004.

[28] M. G. Moharam, E. B. Grann, and D. A. Pommet, and T. K. Gaylord, “Formulation for stable and efficient implementation of the rigorous coupled-wave analysis of binary gratings,” J. Opt. Soc. Am. A., vol. 12, no. 5, pp. 1068-1076, May. 1995.

[29] V. Jovanovic, S. Ghamaty, and J. C. Bass, “New thermoelectric materials and applications,” 13th IEEE ITHERM Conference.

[30] M. Strasser, R. Aigner, M. Franosch and G. Wachutka, “Miniaturized thermoelectric generators based on poly-Si and poly-SiGe surface micromaching,” Sens. Actuators A., vol. 97-98, pp. 535-542, 2002.

[31] Y. Laghla and E. Scheid, “Optical study of undoped, B or P-doped polysilicon,” Thin solid films, vol. 306, pp. 67-73, Apr. 1997.

[32] S. Basu, B. J. Lee, and Z. M. Zhang, “Infrared radiation properties of heavily doped silicon at room temperature,” ASME J. Heat Transfer., vol. 132, pp. 023301-1─023301-8, Feb. 2010.

[33] P. Vincent and M. Neviere, “Corrugated dielectric waveguides: A numerical study of the second-order stop bands,” Appl. Phys., vol. 20, no. 4, pp. 345-351, Dec. 1979.

[34] L. Mashev and E. Popov, “Zero order anomaly of dielectric coated gratings,” Opt. Comm., vol. 55, no. 5, pp. 377-380, Oct. 1985.

[35] I. A. Avrutsky and V. A. Sychugov, “Reflection of a beam of finite size from a corrugated waveguide,” J. Mod. Opt., vol. 36, no. 11, pp. 1527-1539, Jan. 1989.

[36] D. Rosenblatt, A. Sharon, and A. A. Friesem, “Resonant grating waveguide structures,” IEEE J. Quan. Elec., vol. 33, no. 11, pp. 2038-2059, Nov. 1997.

[37] T. K. Gaylord and M. G. Moharam, “Analysis and application of Optical Diffraction by Gratings,” Proc. IEEE, vol. 73, no. 5, pp. 894-937, May 1985.

[38] R. Magnusson, Y. Ding, K. J. Lee, D. Shin, P. S. Priambodo, P. P. Young, and T. A. Maldonado, “Photonic devices enabled by waveguide-mode resonance effects in periodically modulated films,” Proc. SPIE, vol. 5225, pp. 20-34, Oct. 2003.

[39] I. Avrutsky, and R. Rabady “Waveguide grating mirror for large-area semiconductor lasers,” Opt. Lett., vol. 26, no. 13, pp. 989-991, July 2001.

[40] Y. Li, I. R. Srimathi, R. H. Woodward, A. J. Pung, M. K. Poutous, R. K. Shori and Eric G. Johnson, “Guided-Mode Resonance Filters for Wavelength Selection in Mid-Infrared Fiber Lasers,” IEEE Photon. Technol. Lett., vol. 24, no. 24, pp. 2300-2302, Dec. 2012.

[41] N. Matsuyama, Y. Kanamori, J. S. Ye and K. Hane, “Micromachined surface emitting dye laser with a self-suspended guided-mode resonant grating,” J. Opt. A: Pure Appl. Opt., vol. 9, no. 10, pp. 940-944, Oct. 2007.

[42] S. S. Wang and R. Magnusson, “Theory and applications of guided-mode resonance filters,” Appl. Opt., vol. 32, no. 14, pp. 2606-2613, May 1993.

[43] D. Wawro, S. Tibuleac, R. Magnusson, and H. Liu, “Optical fiber endface biosensor based on resonances in dielectric waveguide gratings,” in Proc. SPIE, Biomedical Diagnostic, Guidance, and Surgical-Assist Systems II, San Jose, Calif., vol. 3911, pp. 86-94, May 2000.

[44] R. Magnusson, “Spectrally dense comb-like filters fashioned with thick guided-mode resonant gratings,” Opt. Lett., vol. 37, no. 18, pp. 3792-3794, Sept. 2012.

[45] D. Wawro, S. Tibuleac, R. Magnusson, and H. Liu, “Optical fiber endface biosensor based on resonances in dielectric waveguide gratings,” Proc. SPIE., vol. 3911, pp. 86-94, 2000.

[46] B. E. A. Saleh and M. C. Teich, Fundamentals of Photonics, Hoboken: John Wiley & Sons, 2007.

[47] T. J. Kippenberg, R. Holzwarth and S. A. Diddams, “Microresonator-Based Optical Frequency Combs,” Science, vol. 332, pp. 555-559, 2011.

[48] Z. Zou, L. Zhou, X. Li, and J. Chen, “Channel-spacing tunable silicon comb filter using two linearly chirped Bragg gratings,” Opt. Express, vol. 22, pp. 19513-19522, 2014.

[49] Z. Zhao, M. Tang, H. Liao, G. Ren, S. Fu, F. Yang, P. P. Shum, and D Liu, “Programmable multi-wavelength filter with Mach-Zehnder interferometer embedded in ethanol filled photonic crystal fiber,” Opt. Lett., vol. 39, pp. 2194-2197, 2014.

[50] X. Sun, L. Zhou, J. Xie, Z. Zou, L. Lu, H. Zhu, X. Li, and J. Chen, “Tunable silicon Fabry–Perot comb filters formed by Sagnac loop mirrors,” Opt. Lett., vol. 38, pp. 567-569, 2013.

[51] P. Vincent and M. Neviere, “Corrugated dielectric waveguides: A numerical study of the second-order stop bands,” Appl. Phys., vol. 20, pp. 345-351, 1979.

[52] L. Mashev and E. Popov, “Zero order anomaly of dielectric coated gratings,” Opt Commun, vol. 55, pp. 377-380, 1985.

[53] A. Avrutsky and V. A. Sychugov, “Reflection of a beam of finite size from a corrugated waveguide,” J. Mod. Opt., vol. 36, pp. 1527-1539, 1989.

[54] S. S. Wang and R. Magnusson, “Theory and applications of guided-mode resonance filters,” Appl. Opt., vol. 32, pp. 2606-2613, 1993.

[55] T. K. Gaylord and M. G. Moharam, “Analysis and application of Optical Diffraction by Gratings,” Proc. IEEE, vol. 73, pp. 894-937, 1985.

[56] D. Rosenblatt, A. Sharon, and A. A. Friesem, “Resonant grating waveguide structures,” IEEE J. Quan. Electron., vol. 33, pp. 2038-2059, 1997.

[57] D. Shin, S. Tibuleac, T. A. Maldonado, and R. Magnusson, “Thin film optical filters with diffractive elements and waveguides,” Opt. Eng., vol. 37, pp. 2634-2646, 1998.

[58] R. Magnusson, “Spectrally dense comb-like filters fashioned with thick guided-mode resonant gratings,” Opt. Lett., vol. 37, pp. 3792-3794, 2012.

[59] G. Chen, J. W. Yoon, K. J. Lee, P. Young, and R. Magnusson, “Experimental demonstration of a mode-competing multiline resonant laser,” ,” IEEE Photon. Technol. Lett., vol. 26, pp. 1637-1640, 2014.

[60] D. Liu, S. Fu, M. Tang, P. Shum, and D. Liu, “Comb filter-based fiber-optic methane sensor system with mitigation of cross gas sensitivity,” J. Lightwave Technol., vol. 30, pp. 3103–3108, 2012.

[61] J. Ye, “High finesse Fabry–Perot filter for the measurement of methane gas by using multiline absorption spectroscopy,” Opt. Eng., vol. 53, pp. 024103-1−024103-4, 2014.

[62] Y. Zhang, E. Xu, D. Huang, and X. Zhang, “All-Optical Format Conversion From RZ to NRZ Utilizing Microfiber Resonator,” IEEE Photon. Technol. Lett., vol. 21, pp. 1202-1204, 2009.

[63] X. Dong, P. Guo, Y. Xie,” All-optical RZ-OOK to NRZ-OOK format conversion based on two-ring resonators,” Optical Fiber Technology, vol. 21, pp. 87–92, 2015.

[64] P. Vincent and M. Neviere, “Corrugated dielectric waveguides: A numerical study of the second-order stop bands,” Appl. Phys., vol. 20, pp. 345-351, 1979.

[65] L. Mashev and E. Popov, “Zero order anomaly of dielectric coated gratings,” Opt Commun, vol. 55, pp. 377-380, 1985.

[66] A. Avrutsky and V. A. Sychugov, “Reflection of a beam of finite size from a corrugated waveguide,” J. Mod. Opt., vol. 36, pp. 1527-1539, 1989.

[67] S. S. Wang and R. Magnusson, “Theory and applications of guided-mode resonance filters,” Appl. Opt., vol. 32, pp. 2606-2613, 1993.

[68] M. G. Moharam, E. B. Grann, and D. A. Pommet, and T. K. Gaylord, “Formulation for stable and efficient implementation of the rigorous coupled-wave analysis of binary gratings,” J. Opt. Soc. Am. A., vol. 12, no. 5, pp. 1068-1076, May. 1995.

[69] T. Khaleque, H. Svavarsson, and R. Magnusson, “Fabrication of resonant patterns using thermal nano-imprint lithography for thin-film photovoltaic applications,” Optics Express—Energy, vol. 21, pp. A631-A641, 2013.

[70] G. Chen, J. W. Yoon, K. J. Lee, P. Young, and R. Magnusson, “Experimental demonstration of a mode-competing multiline resonant laser,” ,” IEEE Photon. Technol. Lett., vol. 26, pp. 1637-1640, 2014.

[71] D. Wawro, S. Tibuleac, R. Magnusson, and H. Liu, “Optical fiber endface biosensor based on resonances in dielectric waveguide gratings,” Proc. SPIE., vol. 3911, pp. 86-94, 2000.

[72] Y. Zhang, E. Xu, D. Huang, and X. Zhang, “All-Optical Format Conversion From RZ to NRZ Utilizing Microfiber Resonator,” IEEE Photon. Technol. Lett., vol. 21, pp. 1202-1204, 2009.

[73] X. Dong, P. Guo, Y. Xie,” All-optical RZ-OOK to NRZ-OOK format conversion based on two-ring resonators,” Optical Fiber Technology, vol. 21, pp. 87–92, 2015.

[74] H. Cao, X. Shu, J. Atai, A. Gbadebo, B. Xiong, T. Fan, H. Tang, W. Yang, and Y. Yu, “Optimally-designed single fiber Bragg grating filter scheme for RZ-OOK/DPSK/DQPSK to NRZ-OOK/DPSK/DQPSK format conversion,” Opt. Express, vol. 22, pp. 30442-30460, 2014.

[75] E. Ip and J. M. Kahn,” Power Spectra of Return-to-Zero optical Signals,” J. Lightwave Technol., vol. 24, pp. 1610–1618, 2006.

[76] Alan V. Oppenheim, Signals and systems, Prentice Hall, 1997.

Biographical Information

Guoliang Chen was born in Hunan, China. Guoliang Chen received his B.E. in Microelectronics and Solid-State Electronics from the University of Electronic Science and Technology of China in 2001. He received his M.S. in Microelectronics from the Peking University, China in 2004. He received his Ph.D in Electrical Engineering from the University of Texas at Arlington in 2015.

His research interests include guided-mode resonance optical devices design and fabrication.